Università degli Studi di Padova

Centro interdipartimentale "Centro Ricerche Fusione"

Universidade de Lisboa

Instituto Superior Técnico (IST)

JOINT RESEARCH DOCTORATE IN FUSION SCIENCE AND ENGINEERING

Cycle XXX

Advanced Thomson scattering techniques as diagnostics for fusion plasmas

Candidate: Oisín McCormack

Coordinator: Prof. Paolo Bettini

Supervisor: Prof. Leonardo Giudicotti

Padova, October 2017

ABSTRACT

The content of this thesis was carried out within the framework of the global magnetic confinement fusion (MCF) effort. The flagship project for MCF is the International Thermonuclear Experimental Reactor (ITER), currently under construction and due for commissioning in 2025. ITER is an unprecedented device that pushes the limits of technology and physics across all sectors, and the field of plasma diagnostics is no exception.

Thomson scattering (TS) is one of the most powerful diagnostics available to fusion devices, providing high resolution spatial and temporal profiles of the plasma electron temperature and electron density, which are measurements vital to the understanding of the plasma. Although conventional TS is a well proven method and used in almost all MCF devices in current operation, it too must advance and adapt to the demanding environment of ITER. In this thesis we explore two advanced Thomson scattering techniques which aim to address some of the challenges of ITER TS, through three independent experiments performed on three separate devices.

Chapter 1 provides a brief introduction to MCF as part of the solution to the current global energy crisis.

Chapter 2 introduces the general theory of Thomson scattering and a description of the advanced techniques under investigation.

Chapter 3 describes the dual-laser TS experiment performed in RFX-mod, Padova, during the first year of the PhD. To the author's knowledge, this was the first successful practical testing of this advanced technique.

Chapter 4 describes the polarimetric TS experiment performed in JET, Oxford, during the second year of the PhD. To the author's knowledge, this was the first successful practical testing of this advanced technique.

Chapter 5 describes the dual-laser TS experiment performed in LHD, Japan, during the second year of the PhD. To the author's knowledge, this was the second successful practical testing of this technique.

The experiments performed and described in this thesis demostrate the feasibility of these two previously untested advanced TS techniques, which are both of great interest for application in the next generation of fusion devices.

SOMMARIO

I contenuti di questa tesi sono stati svolti nella cornice della ricerca globale sulla Fusione nucleare a Confinamento Magnetico (FCM). Il progetto guida per la FCM è ITER (International Thermonuclear Experimental Reactor), in costruzione a Cadarache, nel sud della Francia, e con messa in esercizio prevista per il 2025. ITER è una macchina senza precedenti, che spinge all'estremo i limiti della tecnologia e della scienza in tutti i settori, e il campo della diagnostica di plasma non fa eccezione.

Lo scattering Thomson (ST) è una delle diagnostiche più potenti tra quelle disponibili su una macchina a fusione, ed è in grado di misurare con elevata risoluzione spaziale e temporale la temperatura e la densità degli elettroni, misure chiave per lo studio dei plasmi. Sebbene lo ST sia una diagnostica già collaudata e in uso su quasi tutte le macchine a fusione esistenti, anch'esso deve essere migliorato e reso adatto agli esigenti requisiti di ITER. In questo lavoro di tesi sono state esplorate due tecniche di scattering Thomson avanzato che hanno lo scopo di risolvere alcune delle sfide dello ST di ITER attraverso tre esperimenti indipendenti svolti su tre macchine separate.

Capitolo 1 fornisce una breve introduzione alla FCM vista come parte della soluzione all'attuale crisi globale dell'energia.

Capitolo 2 introduce la teoria generale dello scattering di Thomson e una descrizione delle tecniche avanzate trattate in questo lavoro di tesi.

Capitolo 3 descrive l'esperimento di ST con laser duale svolto su RFX-mod, Padova, durante il primo anno di dottorato. Questo è stato per l'autore il primo esperimento svolto con successo su questa tecnica avanzata.

Capitolo 4 descrive l'esperimento di ST polarimetrico svolto su JET, Oxford, durante il secondo anno di dottorato. Questo è stato per l'autore il primo esperimento svolto con successo su questa tecnica avanzata.

Capitolo 5 descrive l'esperimento di ST con laser duale svolto su LHD, Giappone, durante il secondo anno di dottorato. Questo è stato per l'autore il secondo esperimento svolto con successo su questa tecnica avanzata.

Gli esperimenti svolti, descritti in questo lavoro di tesi, dimostrano la fattibilità di queste due tecniche di ST avanzato, mai testate prima, e che sono entrambe di grande interesse per l'applicazione sulla prossima generazione di macchine a fusione.

RESUMO

O conteúdo desta tese foi realizado dentro do programa de esforço global para fusão por confinamento magnético (do inglês, magnetic confinement fusion - MCF). O projeto emblematico desse programa é o “International Thermonuclear Experimental Reactor” (ITER), atualmente em construção e com previsão de comissionamento para 2025. O ITER é um dispositivo sem precedentes que impulsiona os limites da tecnologia e da física em todos os setores - o campo do diagnóstico de plasma não é exceção.

O espalhamento Thomson é um dos mais poderosos diagnósticos disponíveis aos dispositivos de fusão, fornecendo perfis de temperatura e densidade eletrônica do plasma com alta resolução espacial e temporal, que são medidas vitais para sua melhor compreensão. Embora o espalhamento Thomson convencional seja um método bem testado e usado em quase todos os dispositivos de confinamento magnético atualmente em operação, avanços devem ser feitos para adaptá-o ao ambiente exigido pelo ITER. Nessa tese, exploramos duas tecnicas avançadas de espalhamento Thomson que visam abordar alguns dos desafios desse diagnostico para o ITER, através de três experimentos independentes realizados em três dispositivos distintos.

Capitulo 1 fornece uma breve introdução ao MCF como parte da solução atual da crise energética global.

Capitulo 2 introduz a teoria geral do espalhamento Thomson e fornece uma discrição das técnicas avançadas sob investigação.

Capitulo 3 descreve o experimento de laser duplo realizado no RFX-mod, Padova, durante o primeiro ano do doutorado. Pelo conhecimento do autor, esse foi o primeiro teste prático bem sucedido desta técnica avançada.

Capitulo 4 descreve o experimento de espalhamento Thomson polarimétrico realizado no JET, Oxford, durante o segundo ano do doutorado. Pelo conhecimento do autor, esse foi o primeiro teste prático bem sucedido desta técnica avançada.

Capitulo 5 descreve o experimento de espalhamento Thomsom com laser duplo realizado no LHD, Japão, durante o segundo ano do doutorado. Pelo conhecimento do autor, esse foi o segundo teste prático bem sucedido desta técnica avançada.

Os experimentos realizados e descritos nessa tese demonstram a viabilidade dessas duas técnicas avançadas, e não testadas anteriormente, de espalhamento Thomson, ambas de grande interesse para a próxima geração de dispositivos de fusão.

For my parents, Kevin and Ann, this is a culmination of your work as much as mine. A testament to your unconditional support and encouragement at every step of my education, from first words to doctoral thesis.

ACKNOWLEDGMENTS

A sincere thanks to

My supervisor, Leonardo Giudicotti, whose ever-present support and guidance has made the whole PhD an enjoyable and stress-free working experience.

Roberto Pasqualotto and Alessandro Fassina, for all their support and aid at various stages throughout the past three years.

Paulo Bettini, for all of his help and advice as course coordinator, and for supporting me in my scientific communication efforts.

Mark Kempenaars and Joanne Flanagan, for the host of work they have done, their kindness, and for all the interesting conversations over custard.

E. Yatsuka, H. Funaba, I. Yamada, and R. Yasuhara, for their invitation, generosity of time, and remarkable hospitality.

My classmates and office mates, for all the good times and stressful times shared.

Emma, you lift me up with your love and challenge me to climb the mountain, to be a better man.

TABLE OF CONTENTS

Chapter Page

CHAPTER 1: INTRODUCTION

This chapter discusses the global energy scenario and the need for a clean, reliable, large-scale energy source. We introduce fusion energy as the possible solution to humanity's energy needs, and briefly review the history and development of fusion devices.

1.1 The energy scenario

The world consumption of energy continues to rise alongside global population and standard of living. This booming requirement is particularly evident in Asian countries and developing nations [1]. This coincides with the increasingly visible effects of climate change, with for example the U.S. seeing record breaking hurricanes and wildfires in 2017.

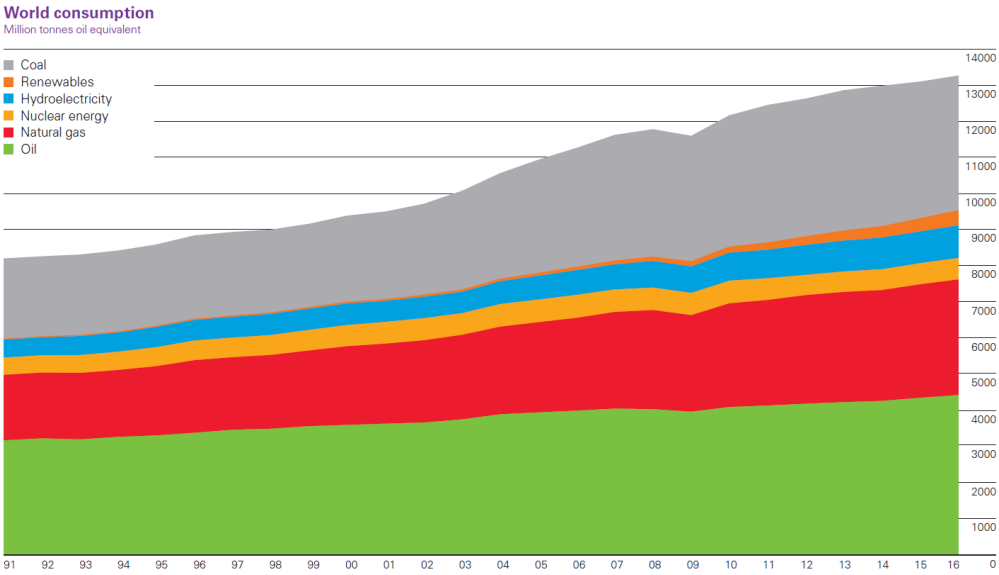

Figure 1 The increasing world energy consumption **[1]**.

Coal remains a very cheap and reliable source of large scale energy, especially evident in Asia which accounts for around 75% of the world consumption of coal [1].

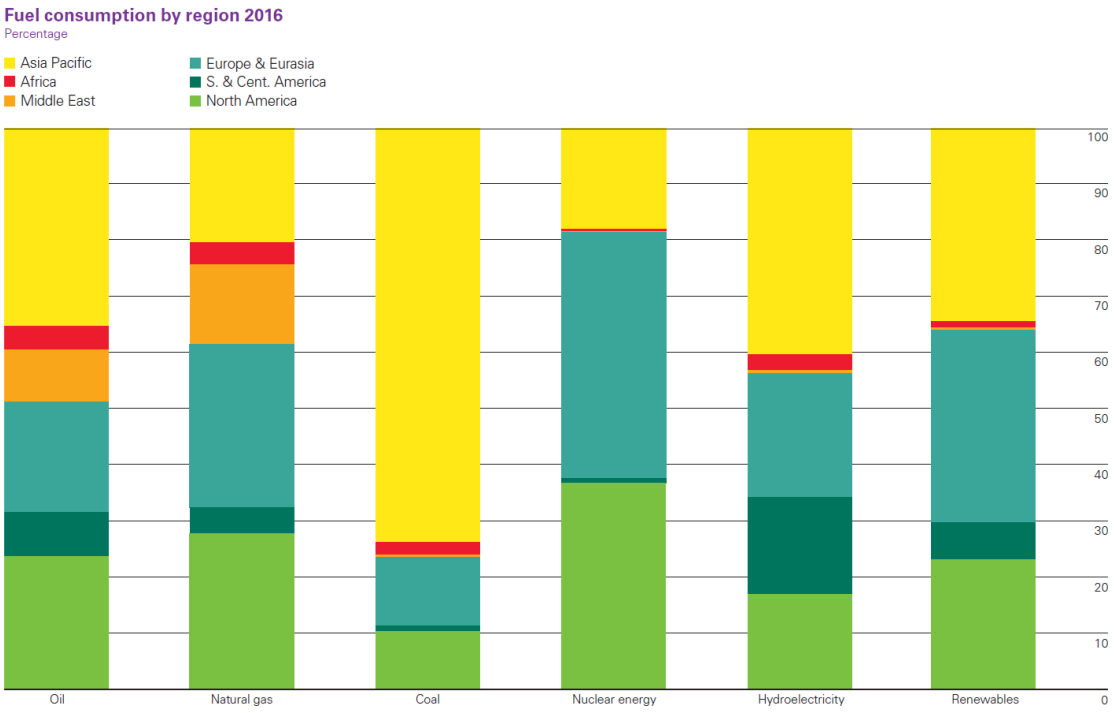

Figure 2 The world fuel consumption by region **[1]**.

Large populations demand energy growth, which leads to using fossil fuel natural resources as a proven and stable energy supply. This however has leads to further increases in fossil fuel greenhouse gas emissions, causing increasing global temperature.

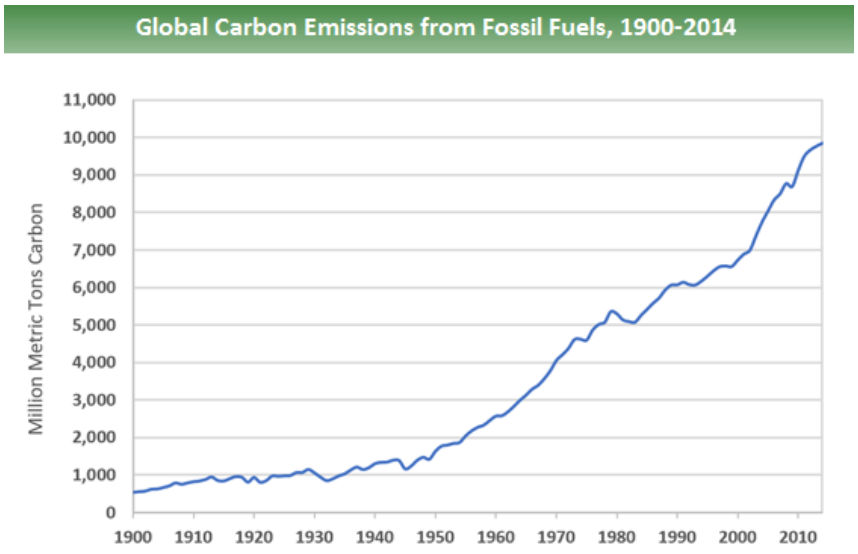

Figure 3 Historic global carbon emissions from fossil fuels **[2]**.

The 2015 Paris Climate Agreement is an historic international accord to tackle climate change. Supported by 194 countries and the European Union, the agreement recognizes the importance of severely reducing greenhouse gas emissions with an aim to limit the global temperature increase to less than 2 °C above pre-industrial levels [3]. To achieve this, a great shift away from fossil fuel usage towards cleaner energy is needed.

Low emission energy technologies include renewable energies such as solar, wind, and hydroelectric, along with nuclear energy. Although the uptake in renewable technologies is increasing, they have several drawbacks regarding limited production locations, reliability and low energy density. Nuclear fission is the only current available energy source that is both low in carbon emission and reliable enough to provide the same type of large scale energy baseline that fossil fuels produce. It is limited however by the relatively rare uranium and plutonium fuel source, the dangers of fission waste and potential nuclear accidents, and a very poor general public opinion.

Nuclear fusion appears as the perfect solution to all of these problems. The fuel source is clean and practically limitless, with deuterium being extracted from seawater and tritium produced in situ from common lithium. There is no “nuclear waste” as the product of the fusion reaction is harmless helium, and the fusion process cannot produce runaway chain reactions that lead to disaster in fission. Fusion is energy-dense, with no issues regarding fuel supply or production location. If successfully harnessed and controlled, fusion could directly replace fossil fuels as the primary source of electricity generation globally.

1.2 The development of fusion energy

In 1939, Hans Bethe verified the theory of proton fusion being the primary heating process in the Sun, through his work on beta decay and quantum tunneling [4]. This idea of obtaining massive amounts of energy from fusion was quickly picked up by the Manhattan Project in the search for a more powerful nuclear bomb, or Hydrogen Bomb as it would later be known. Although the first H-bomb would not see testing until the early 50’s [5], the immediate post-WWII-era began the hunt to control man-made fusion as an energy source.

The first attempts at reactor design were based on a cylindrical linear pinch setup, which sought to squeeze a column of plasma to fusion conditions using current-generated magnetic fields. A fusion plasma is essentially a super-heated electrified gas, where the electrons are not bound to the gaseous particles. This design was presented with many problems however, the principal one being end losses - plasma escaping from each end of the cylinder. And so scientists across the globe started to come up with varying approaches and designs for harnessing this holy grail of energy generation. The desire and need to solve this problem even generated one of the most famous cases of pathological science through the "discovery" of Cold Fusion.

After years of frustrating technological limitations, the world's scientists are currently pursuing two methods: Inertial Confinement Fusion (ICF) and Magnetic Confinement Fusion (MCF). ICF uses high powered lasers to rapidly ignite very small fusion fuel pellets, creating mini fusion explosions. MCF uses strong magnets to confine a large heated plasma over a much longer period. Within MCF are two major design types that provide the most promise for controlled fusion: stellarators and tokamaks.

1.3 Tokamaks

In the early 1950's, behind the veil of the Iron Curtain, Soviet scientists Igor Tamm and Andrei Sakharov came up with a solution to avoid the end losses seen in the standard linear pinch – get rid of the ends by bending the cylinder into a circle and joining them. They decided upon this 'doughnut' shaped and called it a tokamak, an acronym derived from the Russian translation of 'toroidal chamber with magnetic coils', using poloidal and toroidal magnetic fields to confine and shape the plasma. However a curved plasma path presented its own problem in the form of particle drift away from the core. To correct for this, the Russians induced an electric field in the plasma which in turn produces a transient poloidal field. These fields then all act together to create a twisting magnetic field which counteracts charged particle drift, as the particles are confined to gyrate tightly along these helical field lines. Figure 4 shows us the various magnetic forces involved in a tokamak and the resulting helical magnetic field produced.

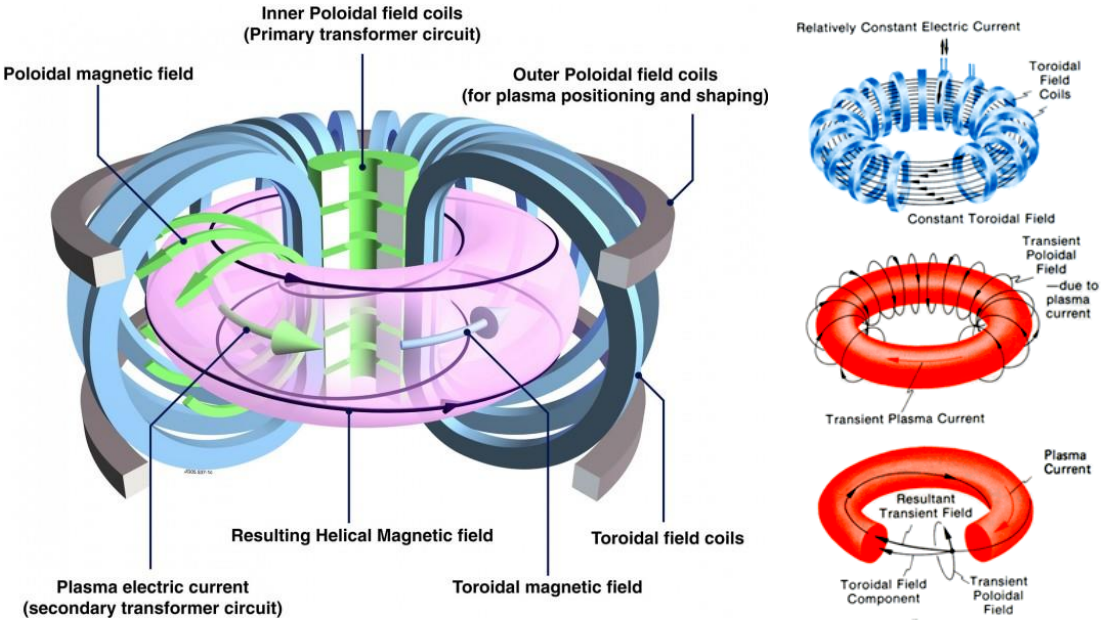

Figure 4 (Left) The standard tokamak design **[6]**, and (right) how the different components shape the overall helical magnetic field **[7]**.

The first tokamaks boasted a confinement much greater than other designs of the time, and so after general declassification of fusion research a team of British scientists tested the Soviet device and overnight the plans for new tokamak projects were drafted all over the world. Many technological and engineering mountains would have to be scaled to reach a usable end product. These included requiring reactor wall material that could withstand a massive heat load, eradicating plasma impurities, and managing a swathe of instabilities arising from inside the plasma [8].

Unfortunately, the method of using an induced electric field to help contain the plasma is also one of the primary sources of instability in a tokamak, and the pulsed nature of this current means that the tokamak design with induced field can never be operated in a steady state mode.

Despite this, tokamaks are the most developed of all MCF reactor designs. From humble beginnings with reactor major radii on the scale of 1 metre, and a far cry from usable fusion, the global scientific community has now come together to create the impressive International Thermonuclear Experimental Reactor (ITER) project. ITER is expected to be the first MCF reactor to not only breakeven, but will produce 10 times more energy

output than input required for approximately 500MW capacity, comparable to large fossil fuel power stations [9].

1.4 Stellarators

In parallel with the Russians, Lyman Spitzer had a truly unique idea at his Princeton laboratory – the stellarator. Spitzer's first device incarnation was to take the toroidal doughnut design, stretch it, and fold it into a figure-eight. This in theory would provide the same helical path necessary to counteract particle drift that is provided by the tokamak, but importantly without the need to induce a plasma current, giving for an all magnetic design. This vital difference provided the possibility of steady state operation as well as avoiding the host of major instabilities caused by current induction.

These advantages came at a price, namely that stellarators are not azimuthally symmetric like the tokamak. This then brings design from essentially 2D into a fully 3D process, giving a plasma with up to 50 degrees of freedom as opposed to the tokamak's 4 degrees [10]. This gave a level of complexity to the design process that was far beyond the ability of computers and machining technology of the era. Thus despite increasing effectiveness with varying design concepts, stellarators quickly became overshadowed by their relatively less complicated tokamak cousins for several decades.

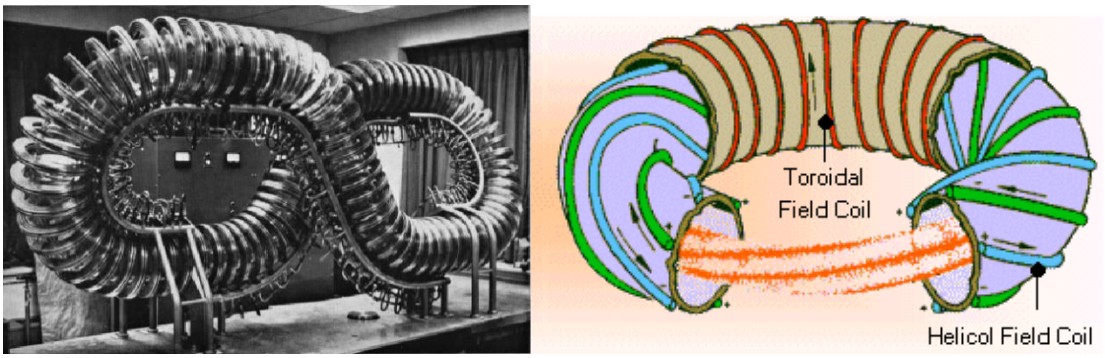

Figure 5 Early stellarator designs – Spitzer's figure-8 **[11]** and the first torsatrons **[12]** – could not provide the precision required for plasma confinement in non-azimuthally symmetric systems.

It’s not until recent years that computational design and manufacturing have caught up with the heavy design requirements of stellarators. Modern day stellarators, like the German Wendelstein 7-X, make full use of current 3D design technology, pushing it to its limits.

The W 7-X – commissioned in 2015 – employs a series of 50 modular non-planar and 20 planer superconducting magnetic coils to contain a stable plasma. Although not large enough to obtain ITER power outputs, by 2021 W 7-X aims to produce a 30 minute thermal plasma discharge, a duration only limited by the cooling power of the system [13]. This is a marketed advantage over the expected ITER pulse durations of 8 minutes.

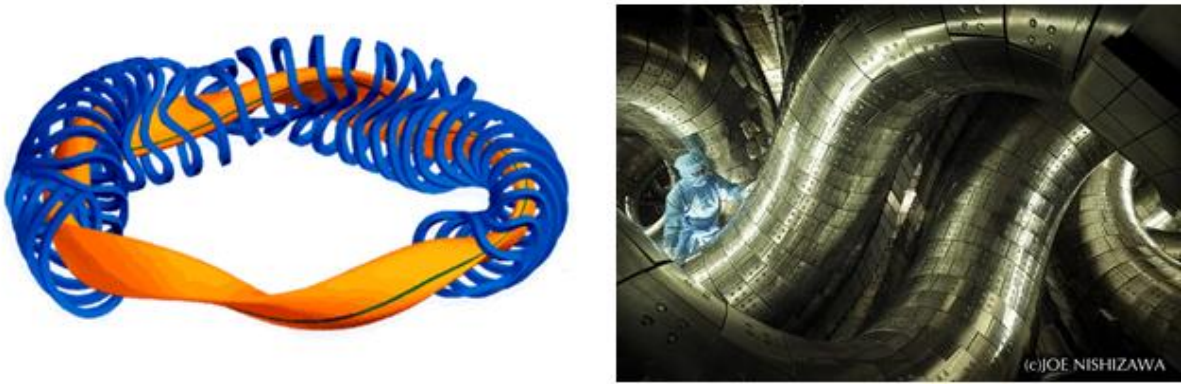

Figure 6 (Left) The non-planer coils will produce a complicated but stable plasma for W 7-X **[14]**. (Right) The otherworldly insides of Japan’s LHD stellarator **[15]**.

1.5 Plasma heating

The ultimate goal for commercial MCF is to reach ignition and generate a ‘burning plasma’. This is where a portion of the nuclear energy created is used to maintain the plasma at fusion temperatures, essentially becoming self-sustaining. However, to reach these high temperatures (~150 million °C) in the first place, we need to initially provide the heating energy from other sources.

As mentioned previously, in a tokamak an electric current is induced in the plasma via the central solenoidal transformer. This current serves a dual purpose; it creates the poloidal magnetic field which helps to shape and confine the plasma, while also generating heat via ohmic heating. Ohmic heating is the standard form of resistive

electric heating we see every day in electric kettles and filament light bulbs. This turned out to be very efficient at lower temperatures but once past temperatures in the range of 50 million °C the plasma resistivity drops and the current simply cannot heat it past this point [16].

The ultimate limitations of ohmic heating led to the creation of two new heating techniques totally independent of the current. The first method, known as Radio Frequency (RF) heating, uses high-frequency electromagnetic waves generated in an oscillator situated outside of the torus. This acts to heat the plasma in a similar way that a microwave oven heats food. Different RF heating machines can be targeted to heat either the ions or the electrons inside the plasma by using an appropriate emission frequency for the radiation.

The second method, called Neutral Beam (NB) heating is essentially neutral deuterium atoms that are injected into the tokamak plasma at high speeds. These atoms have large kinetic energies, which they share with the plasma via collisions with the already present particles, hence increasing the overall energy and temperature. Ohmic, NB, and RF heating are all used in heating a tokamak plasma, while the latter two are the primary sources of heating for a stellarator setup. Recording and analyzing these extreme temperatures is vital for almost all fusion plasma experiments.

1.6 Fusion diagnostics

Plasma physics has been established as a relatively new major area of research. Understanding plasma behavior is key to developing successful fusion scenarios, and in order to do this we rely on comparing practical measurements of plasma properties with our adapting theoretical models. These measurements must necessarily be as accurate as possible and so developing and employing plasma diagnostics is a wide branching area of research. Fusion plasmas present a particularity unique challenge due to the extreme temperatures involved and many novel techniques have been invented and see continued development.

Plasma diagnostics usually measure a particular plasma property or process, such as the plasma particle flux, refractive index, line radiation, plasma magnetic fields, the emission and scattering of electromagnetic waves. Each measured property can give us information on more than one plasma parameter, which include the electron and ion velocity distributions, densities, temperatures, plasma pressure and the electric and magnetic field strengths [17]. ITER will employ about 50 individual diagnostic systems which all provide data on one or more plasma parameters, providing overlapping data sets that together will feed into the working models, giving us the ability to control and predict plasma behavior to enable fusion [13].

Incoherent Thomson scattering (TS), which utilizes electromagnetic waves that are scattered by the plasma, is one of the most reliable and accurate diagnostic methods for determining both the electron temperature and electron density, and is used in practically all fusion experiment devices. In ITER there will be 3 independent Thomson scattering systems providing spatial and temporal profiles of the electron temperature (T_e) and density (n_e) in the edge, the core, and the divertor regions of the plasma. The core plasma Thomson scattering (CPTS) system is particularly challenging due to the very high plasma conditions ($T_e \leq$ 40keV) and the stresses on the experimental equipment due to the nuclear environment.

For this reason, advanced Thomson scattering techniques must be explored to increase the accuracy and performance of the conventional TS setup:

Dual-laser Thomson scattering is a method that utilizes a secondary calibration laser, which could allow for the continuous self-calibration of the CPTS system, increasing the accuracy at high temperatures and avoiding the challenging problem of access for the cumbersome traditional calibration method.

Polarimetric Thomson scattering measures the relativistic depolarization of Thomson scattering, providing a unique measurement of T_e independent of wavelength, which could significantly increase the accuracy of the system at very high temperatures.

This thesis presents three experiments which, to the author's knowledge, are the first practical investigations of these two advanced techniques.

CHAPTER 2: THOMSON SCATTERING THEORY

This chapter lays out the foundational theory of Thomson scattering (TS). We look at the conventional TS method before describing the theory of the two advanced TS techniques, dual-laser TS and polarimetric TS, which are the basis for the three experiments described in this thesis.

2.1 Thomson scattering

One of the most powerful methods of plasma diagnostics is the use of electromagnetic radiation, usually a laser, to be scattered by the plasma. This observed scattering light can give us detailed information on the plasma electron (or ion) density and electron (or ion) temperature, producing high resolution profiles of the plasma. In practice this is a non-perturbing method which only requires access via vacuum windows for the incident and scattered light, although the collection and measurement requires high accuracy and is technically difficult.

The scattering of electromagnetic waves by electrons can be described in two ways. From a classical mechanics standpoint, the electric field of the incident radiation accelerates a free charged particle – in our case an electron -, causing it in turn to emit radiation in all directions (Figure 7). This radiation is the scattered wave, which has been Doppler shifted due to the motion of the electron. This Doppler broadening of the scattered wave frequency depends on the velocity distribution (temperature) of the electron. Figure 8 shows that we can measure the electron temperature from the width of the frequency broadening, with higher temperatures giving for wider profiles. We can also measure the electron density of the plasma from the amount of scattering light received, i.e. the area under the curve. We measure electron scattering because ions are so much heavier that they are not accelerated by the electric field to the same extent, so the ion scattering radiation is nominal and can usually be neglected [17].

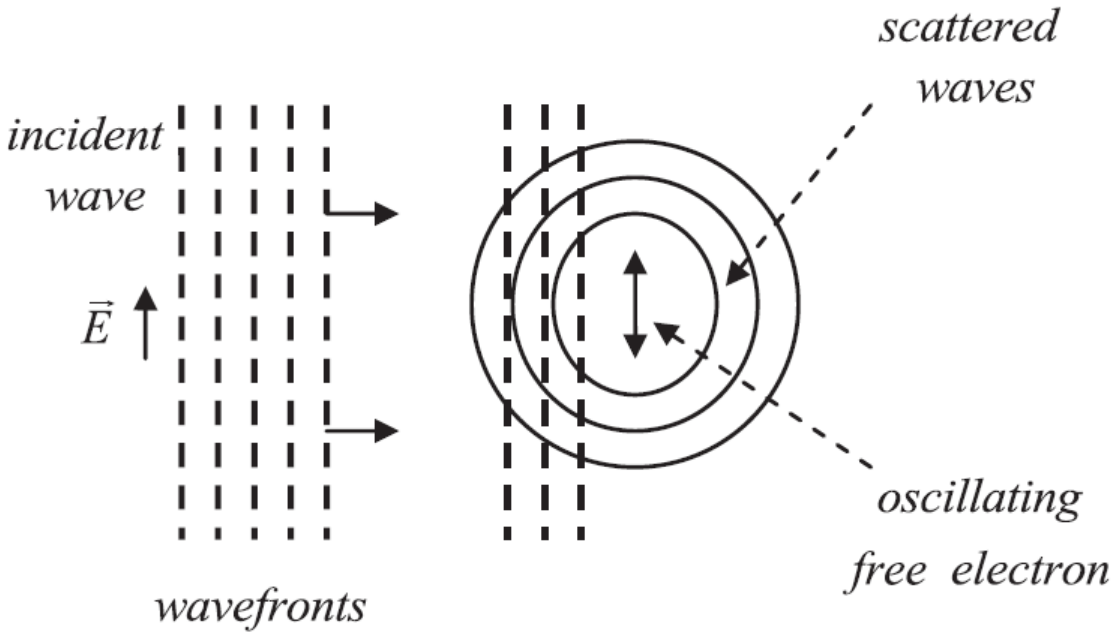

Figure 7 Illustration of the Thomson scattering sentence **[18]**.

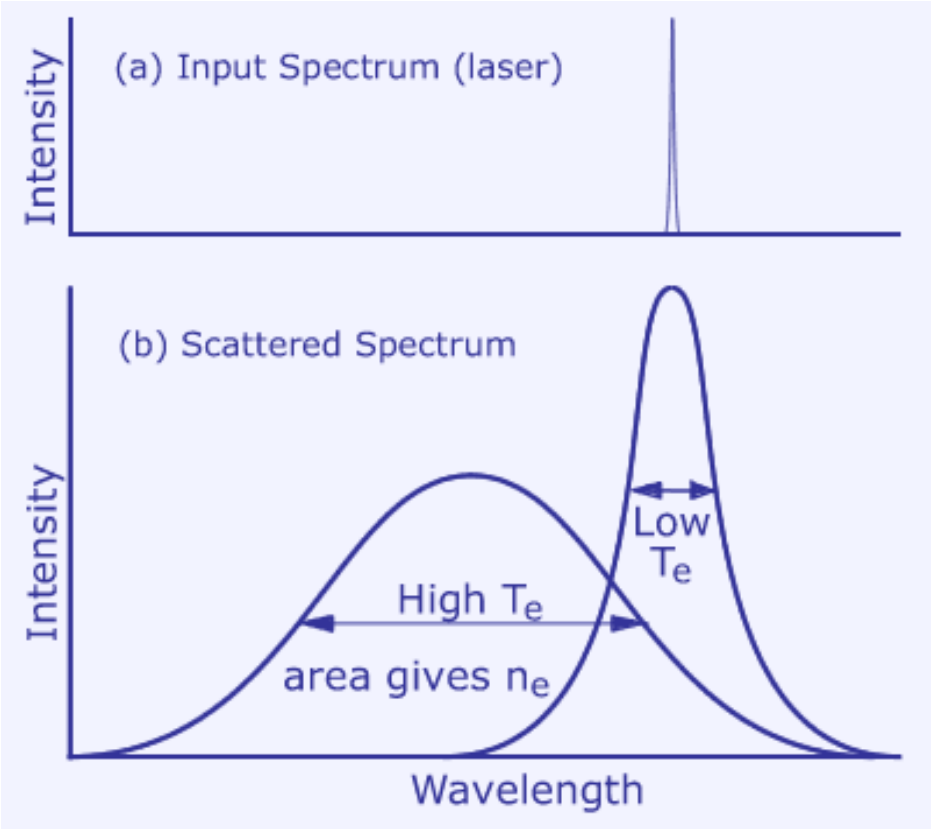

Figure 8 Comparison of input and scattered spectra **[19]**.

Looking from quantum mechanics we can otherwise describe it as the incident photons colliding with the electrons and being deflected away in various directions. This viewpoint would lead to the same mathematical description as the classical version, provided that the photon mass is much smaller than the electron mass ($\hbar\omega \ll mc^2$). This classical limit is known as Thomson scattering, with most Thomson scattering systems using incident photons of $\hbar\omega \approx 1\ eV$ compared to the rest mass of an electron $m_0c^2 = 511\ keV$. When the photons have enough energy that their collision has an effect on the electron momentum, this is known as Compton scattering which will not be discussed here.

2.2 Scattering theory

2.2.1 Scattering from a single electron

We first consider an incident electromagnetic wave in the $\hat{\mathbf{i}}$ direction, scattered by a single free electron in an unperturbed position given by $\boldsymbol{r}(t)$. The incident wave accelerates the electron which emits radiation in all directions, with the scattered radiation wave that is observed being in the $\hat{\mathbf{s}}$ direction of observation. From [17], we have with an electron with velocity $\mathbf{v} = c\boldsymbol{\beta}$ moving in time varying electric and magnetic fields **E** and **B**. The equation of motion is thus

$$\frac{\partial}{\partial t}\left\{\frac{m_0\mathbf{v}}{(1-\beta^2)^{1/2}}\right\} = -e(\mathbf{E} + \mathbf{v}\times\mathbf{B}) \qquad (1)$$

This can be calculated to give

$$m_0\gamma\dot{\boldsymbol{\beta}} + \gamma^3 m_0\boldsymbol{\beta}(\boldsymbol{\beta}\cdot\dot{\boldsymbol{\beta}}) = -e\left(\frac{1}{c}\mathbf{E} + \boldsymbol{\beta}\times\mathbf{B}\right) \qquad (2)$$

where $\gamma = (1-\beta^2)^{-1/2}$ is the relativistic factor, $\dot{\boldsymbol{\beta}} = d\boldsymbol{\beta}/dt$, and m_0 is the electron rest mass. In the nonrelativistic limit, the initial velocity of the electron is very small, $\boldsymbol{\beta} \ll 1$ and $\gamma \approx 1$, so we can simplify the equation of motion to

$$\dot{\boldsymbol{\beta}} = \frac{-e}{m_0 c}\mathbf{E}_i \qquad (3)$$

where $\mathbf{E}_i$ is the incident transverse plane wave in the $\hat{\mathbf{i}}$ direction.

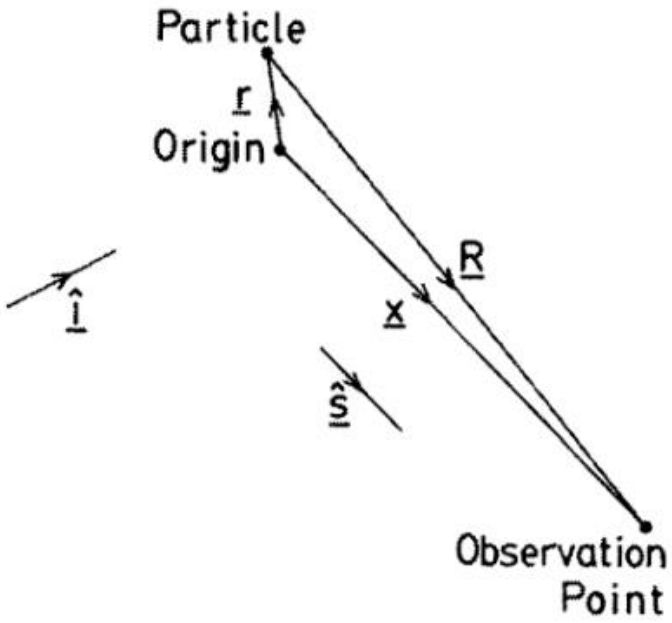

Figure 9. Vector diagram scattering geometry **[17]**.

The radiated scattered electric field in the $\hat{\mathbf{s}}$ direction can be shown [17] as

$$\mathbf{E}_s = \frac{-e}{4\pi\varepsilon_0}\left[\frac{1}{Rc}\left(\hat{\mathbf{s}} \times \left(\hat{\mathbf{s}} \times \dot{\boldsymbol{\beta}}\right)\right)\right] \qquad (4)$$

where R is the distance from the particle to the observation point. Looking at Figure 9, $R \approx x - \hat{\mathbf{s}} \cdot \mathbf{r}$ where $\mathbf{r}$ is the position of the electron relative to an origin in the scattering volume, which is much smaller than the distance x from the origin to the observation point. So we can approximate $\mathbf{R}/R \equiv \mathbf{x}/x$ which is equal to $\hat{\mathbf{s}}$**.** Inserting the value for $\dot{\boldsymbol{\beta}}$ from equation (3) gives

$$\mathbf{E}_s = \left[\frac{r_e}{R}\left(\hat{\mathbf{s}} \times (\hat{\mathbf{s}} \times \mathbf{E}_i)\right)\right] \qquad (5)$$

where $r_e = e^2/4\pi\varepsilon_0 m_0 c^2 = 2.82 \times 10^{-15} m$ is the classical electron radius. The power per unit solid angle (Ω_s) scattered by a single electron in the $\hat{\mathbf{s}}$ direction is given by

$$\frac{dP}{d\Omega_s} = R^2 \varepsilon_0 c |\mathbf{E}_s|^2 \quad (6)$$

Substituting in for $\mathbf{E}_s$ results in

$$\frac{dP}{d\Omega_s} = {r_e}^2 \sin^2 \phi \, \varepsilon_0 c |\mathbf{E}_i|^2 \quad (7)$$

where ϕ is the angle between $\mathbf{E}_i$ and $\hat{\mathbf{s}}$. We define the differential cross section $(d\sigma)$ as the ratio of $dP/d\Omega_s$ to the incident power per unit area $\varepsilon_0 c |\mathbf{E}_i|^2$, giving

$$\frac{d\sigma}{d\Omega_s} = {r_e}^2 \sin^2 \phi \quad (8)$$

Given that $d\Omega_s = 2\pi \sin\phi \, d\phi$, the total Thomson scattering cross section is the integral of equation (8) over all solid angles, giving simply

$$\sigma = \frac{8\pi}{3} {r_e}^2 = 6.65 \times 10^{-29} m^2 \quad (9)$$

This Thomson scattering cross section is purely proportional to the classical electron radius. It can be thought of in simple terms as the area that the electron presents for scattering purposes. In general terms the scattering power and scattering cross section are inversely proportional to the mass of the particle squared, which is why we focus on electron scattering as scattering by the ions in a plasma is negligible due to their much greater mass [20].

To define the incident and scattered waves, consider the electromagnetic wave incident on the electron to be monochromatic, of the form

$$\mathbf{E}_i(\mathbf{r}, t) = \mathbf{E}_i e^{i(\mathbf{k}_i \cdot \mathbf{r} - \omega_i t)} \quad (10)$$

This accelerated electron produces a scattered wave at a distant observation point **x** whose Fourier spectral component at scattered frequency ω_s can be given by [17]

$$\mathbf{E}_s(\omega_s) = \frac{r_e e^{i\mathbf{k}_s\cdot\mathbf{x}}}{x}\int_{T'} \kappa' \prod' \cdot \mathbf{E}_i e^{i(\omega t' - \mathbf{k}\cdot\mathbf{r}')} dt' \qquad (11)$$

where $\omega = \omega_s - \omega_i$ is the scattering frequency and $\mathbf{k} = \mathbf{k}_s - \mathbf{k}_i$ is the scattering wave vector. Primes signify evaluation at the retarded time $t' = t - \frac{1}{c}(x - \hat{\mathbf{s}}\cdot\mathbf{r}')$ and $\kappa' = dt/dt'$ relates normal to retarded time. $\prod$ is a tensor polarization operator that transforms the input wave polarization, $\hat{\mathbf{e}} = \mathbf{E}_i/\mathrm{E}_i$, into scattered wave polarization where [17]

$$\prod \cdot \hat{\mathbf{e}} = \frac{(1-\beta^2)^{1/2}}{\kappa^3}\hat{\mathbf{s}} \times \{[\hat{\mathbf{s}} - \boldsymbol{\beta}] \times [\hat{\mathbf{e}} - (\boldsymbol{\beta}\cdot\hat{\mathbf{e}})\boldsymbol{\beta} + (\boldsymbol{\beta}\cdot\hat{\mathbf{e}})\hat{\mathbf{i}} - (\boldsymbol{\beta}\cdot\hat{\mathbf{i}})\hat{\mathbf{e}}]\} \qquad (12)$$

2.2.2 Scattering in a plasma

Until this point we have discussed an incident wave scattering from a single electron. Now we need to consider a plasma consisting of many scattering electrons, all of which contribute to the overall scattered power. The total scattered field $\mathbf{E}_s$ is given by the sum of the individual electron contributions [20]

$$\mathbf{E}_s = \sum_j \mathbf{E}_j \qquad (13)$$

where $\mathbf{E}_j$ refers to the individual scattering fields of all j number of electrons in the scattering volume. The average scattered power is given by equation (6)

$$\begin{aligned}\frac{dP}{d\Omega_s} &= R^2\varepsilon_0 c|\mathbf{E}_s|^2 \\ &= R^2\varepsilon_0 c\sum_j\sum_e \left|\mathbf{E}_j\cdot\mathbf{E}_e\right| \\ &= R^2\varepsilon_0 c\sum_j \left|\mathbf{E}_j\right|^2 + R^2\varepsilon_0 c\sum_{j\neq e}\left|\mathbf{E}_j\cdot\mathbf{E}_e\right|\end{aligned} \qquad (14)$$

The first term in the final line of equation (14) is simply the summation of the power scattered by each electron independently. The second term represents a contribution due to the collective effect caused by correlations in the electron positions and motions that can be found in a plasma. If the electrons are distributed randomly and thus the phases of all contributions completely uncorrelated, then the second term would be zero.

In a plasma, the Debye shielding effects cause an individual test charge to be surrounded by a cloud of opposite shielding charges (see Figure 10), and so the typical correlation length is the characteristic Debye length λ_D. From equation (11) we see that the phase of the scattering wave contains the term $\mathbf{k} \cdot \mathbf{r}'$ and so the correlation depends on the quantity $k\lambda_D$.

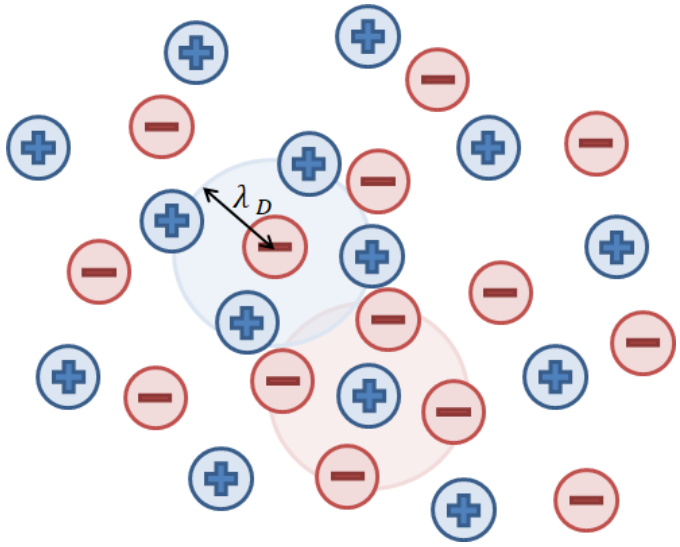

Figure 10 Representation of Debye shielding clouds with radius $\boldsymbol{\lambda_D}$.

If $k\lambda_D \gg 1$, then the phase difference between the scattering from an electron and subsequent scattering from electrons at the distance of its shielding cloud is large, with the phase changing rapidly between scatterings. In this case the scattered fields of the first electron and those in the shield cloud have no correlation, and the second term in equation (14) is negligible. This is called incoherent Thomson scattering, and the total scattered power is a simple sum of the contribution of each individual electron.

On the other hand, when $k\lambda_D \ll 1$, then there is negligible phase difference between scattering electrons, so the correlations between the electrons affect the scattering spectrum. This is called coherent (or collective) Thomson scattering, which depends on

the thermodynamic equilibrium of the plasma and requires the use of plasma kinetic theory to evaluate. As the collective scattering is mainly done by these electron shielding clouds which have a dependence on the ion velocity distribution, the scattered spectra will have an ion feature. This ion feature can be fitted to give us information on the bulk properties of the ions, such as ion temperature and rotation [21]. Collective Thomson scattering is a useful but very separate technique from incoherent Thomson scattering. The experiments described within this thesis are all based on incoherent scattering systems, so we will not discuss collective scattering further here.

2.2.3 Incoherent Thomson scattering

For the following we take the standard assumption that the incident wave electric field $\mathbf{E}_i$ is perpendicular to the scattering plane, and furthermore there is a linear polariser installed between the plasma and the collection fibre optics so that we measure only the scattered field component parallel to $\mathbf{E}_i$, which reduces the signal noise by blocking half of the randomly polarized plasma light. In this case, for incoherent scattering, the scattered power per unit solid angle per unit angular frequency from a volume of electrons of density n_e and velocity distribution $f(\boldsymbol{\beta})$ can be shown [18] to be

$$\begin{aligned}\frac{d^2P}{d\Omega_s d\omega_s} = r_e^2 \int_{vol} \langle S_i \rangle n_e d^3\mathbf{r} \int_{vel} \left(\frac{\omega_s}{\omega_i}\right)^2 \\ \times \left\{1 - \frac{\beta_e^2\left(1 - \hat{\mathbf{s}}\cdot\hat{\mathbf{i}}\right)}{(1-\beta_i)(1-\beta_s)}\right\}^2 (1-\beta^2) \\ \times f(\boldsymbol{\beta})\delta(\mathbf{k}\cdot\mathbf{v} - \omega) d^3\boldsymbol{\beta}\end{aligned} \quad \textbf{(15)}$$

where $\langle S_i \rangle = \varepsilon_0 c|\mathbf{E}_i|^2/2$ is the time-averaged Poynting vector of the incident field, and $\beta_e = \boldsymbol{\beta}\cdot\hat{\mathbf{e}}$ with similar expressions for β_i and β_s. Here the Dirac delta function is given by

$$\delta(\omega_s - \omega_d) = \frac{1}{2\pi}\int_{-\infty}^{+\infty} e^{j(\omega_s - \omega_d)t} dt = \delta(\mathbf{k}\cdot\mathbf{v} - \omega)(1-\beta_s) \quad \textbf{(16)}$$

with $\omega_d \equiv \omega_i\left(\frac{1-\beta_i}{1-\beta_s}\right)$ as the Doppler shifted frequency.

Equation (15) is the formula for determining the scattered spectrum. The term $(\omega_s/\omega_i)^2$ accounts for the Doppler shift in the spectrum. The second term in the curly brackets describes the depolarization of the scattered light. As it is dependent on β_e^2, the depolarization is a relativistic effect which only becomes significant in very hot plasmas [22]. This is a very important effect which is the basis of the polarimetric Thomson scattering technique [23], which will be discussed later.

2.2.4 Practical analytical formulae for the relativistic TS spectrum

For very high temperatures, the higher order β terms in equation (15) must be included. In this case the velocity integral can be calculated analytically, but only by simplifying and approximating the depolarization term as a constant. With this simplification the scattering can be evaluated with a fully relativistic expression described by Zhuravlev and Petrov [24]. The velocity integral, called the spectral density function, becomes a function of $(\epsilon, \theta, 2\alpha)$, where θ is the scattering angle, $2\alpha = m_e c^2/kT_e$, and $\epsilon = (\lambda_s/\lambda_i) - 1$ is the normalized shift in the wavelength of the scattered light, with λ_i as the incident wavelength and λ_s the scattered wavelength. Equation (15) then becomes:

$$\frac{d^2P}{d\Omega_s d\epsilon} = r_e^2 \int_{vol} \langle S_i \rangle d^3\mathbf{r}\, S_Z(\epsilon, \theta, \alpha) \qquad \textbf{(17)}$$

$$S_Z(\epsilon, \theta, \alpha) = \frac{exp(-2\alpha x)}{2K_2(2\alpha)(1+\epsilon)^3}[2(1-cos\theta)(1+\epsilon)+\epsilon^2]^{-1/2} \qquad \textbf{(18)}$$

Where $x = \left(1 + \frac{\epsilon^2}{2(1-cos\theta)(1+\epsilon)}\right)^{1/2}$ and K_2 is the modified Bessel function of the second kind. The subscript Z on $S_Z(\epsilon, \theta, \alpha)$ denotes that this is the spectral density function obtained by Zhuravlev.

This expression was then converted into a simple practical formula by Selden [25], that when calculated agrees with an exact numerical integration [26] to a high degree for practical uses. Selden shows that the scattered power per unit wavelength can be written as the simple product of one function of (ϵ, θ) with the exponential of another. The Selden spectral density function $S_S(\epsilon, \theta, \alpha)$ is given by

$$S_S(\epsilon,\theta,\alpha) = c(\alpha)A^{-1}(\epsilon,\theta)exp[-2\alpha B(\epsilon,\theta)] \quad \textbf{(19)}$$

where

$$A(\epsilon,\theta) = (1+\epsilon)^3[2(1-cos\theta)(1+\epsilon)+\epsilon^2]^{1/2} \quad \textbf{(20)}$$

$$B(\epsilon,\theta) = \{1+\epsilon^2/[2(1-cos\theta)(1+\epsilon)]\}^{1/2} - 1 \quad \textbf{(21)}$$

$$c(\alpha) = (\alpha/\pi)^{1/2}\left(1-\frac{15}{16}\alpha^{-1}+\frac{345}{512}\alpha^{-2}+\cdots\right) \quad \textbf{(22)}$$

when $\alpha \gg 1$, where $c(\alpha)$ is a normalising constant. Equation (19) can be used to determine the relativistic blue shift of the scattering spectrum as a function of T_e. In a practical sense, this can be made into a fitting routine, where the width of the measured scattering spectrum gives us the electron temperature.

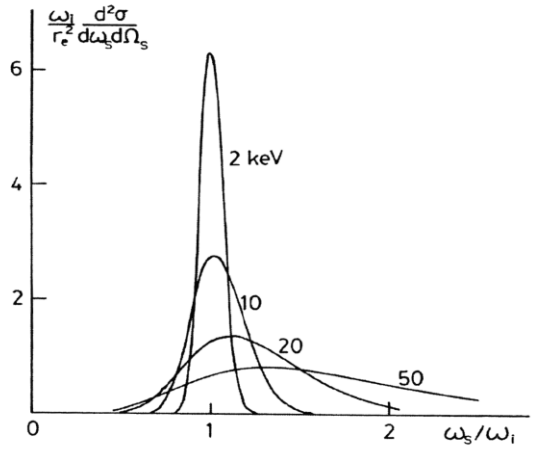

Figure 11. Thomson scattering spectral shapes at varying $\boldsymbol{T_e}$ **[17]**.

This expression agrees with the computational integration and is accurate for practical use up to 100keV, although there is a disparity between the values at the higher temperatures (>20keV). This can be fixed by using a correction factor, tabulated by Selden for 90° scattering. However, if a diagnostic system has multiple scattering angles, the correction factor must be calculated for each angle. This is the case in the Thomson scattering system of RFX-mod, which uses the Selden formula with multiple correction factors.

For ITER it is expected that the Thomson scattering analysis will use a more complete analytical formula described by Naito [27]. This has the inclusion of a depolarization term $q(\epsilon,\theta,\alpha)$ onto the Zhuravlev equation (17), giving the Naito spectral density function $S_N(\epsilon,\theta,\alpha)$ as

$$S_N(\epsilon,\theta,\alpha) = S_Z(\epsilon,\theta,\alpha)q(\epsilon,\theta,\alpha) \qquad \textbf{(23)}$$

The term $q(\epsilon,\theta,\alpha)$ is calculated by considering an incident wave linearly polarized perpendicular to the scattering plane, scattered by a single electron and transformed to a scattering wave via the tensor polarization operator Π of equation (12), and integrating this single electron scattering over the relativistic Maxwell velocity distribution. The formulae and expansion for $q(\epsilon,\theta,\alpha)$ are quite involved and can be found in [27], however final practical form of this depolarization term is given by

$$\begin{aligned}
&q(\epsilon,\theta,\alpha) = 1 - 4\eta\zeta\,\frac{p_0+p_1\eta+p_2\eta}{q_0+q_1\eta+q_2\eta} + O(\eta^6)\,,\\
&p_0 = q_0 = 4 + 30\zeta^2 - 55\zeta^4,\\
&p_1 = -\zeta(24 - 545\zeta^2 + 720\zeta^4),\\
&p_2 = 2(33 - 165\zeta^2 + 240\zeta^4 - 100\zeta^6),\\
&q_1 = 25\zeta^3(29 - 42\zeta^2),\\
&q_2 = 5(18 - 66\zeta^2 + 630\zeta^4 - 805\zeta^6),\\
&\eta = \frac{y}{2\alpha}\quad,\quad \zeta = xy\quad,\quad y = (x^2+u^2)^{-1/2}\quad,\quad u = \frac{\sin\theta}{1-\cos\theta}
\end{aligned} \qquad \textbf{(24)}$$

The Naito expression corrects for the Zhurzvlev depolarization simplification and is accurate to less than 0.1% relative error at 100keV without the need of the Selden corrective factors, and additionally is valid for arbitrary scattering angle. The complete formula requires just simple computations and so is a useful practical tool for Thomson scattering analysis, and accurate in the high temperature range in which ITER will operate [27].

2.3 Conventional Thomson scattering

The most challenging practical aspect of incoherent Thomson scattering is the low amount of collected scattered photons. The fraction of incident light that gets scattered depends on the Thomson cross section $\sigma = 8\pi {r_e}^2/3 = 6.65 \times 10^{-29} m^2$, the electron density n_e, and the length L of plasma that the light passes through. In a typical fusion plasma $\sigma n_e L \approx 10^{-8}$ of the incident photons. An even smaller fraction of the scattered photons are actually detected as the individual collection optics usually focus on a small portion of the plasma length (about 1cm) and have a relatively small solid angle of collection. In the end only about 10^{-13} of the input photons will be collected as scattered photons [17]. In this manner we require to use a high energy and high power light source, which is why energetic laser pulses are used.

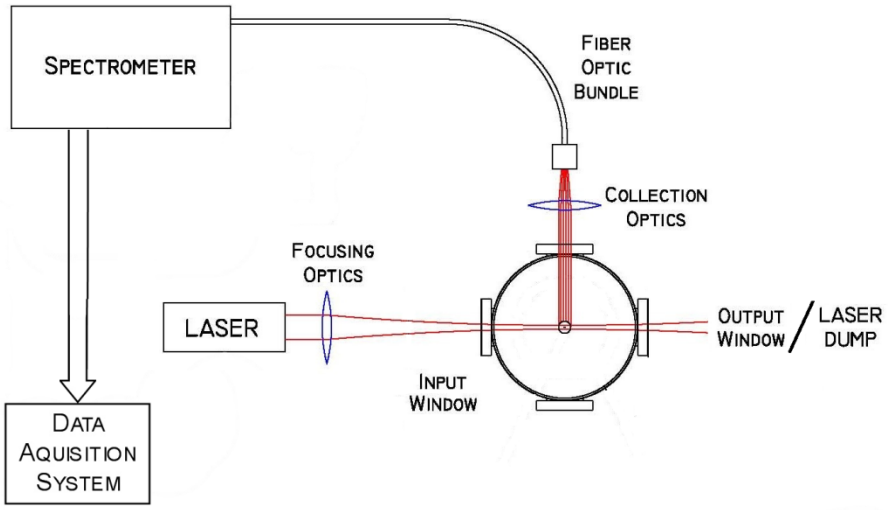

Figure 12. A typical incoherent Thomson scattering experiment setup with 90° scattering.

Although the lasers are powerful enough so that such a small fraction of scattered photons are detectable, further challenges are found in the form of signal noise. The biggest source of noise is stray light, mainly from the powerful laser being scattered by the input vacuum window where it enters the chamber and bounces around as well as reflections from the output window / beam dump. This noise can be orders of magnitude

greater than the Thomson scattering light. Several in-chamber components such as baffles, a viewing dump, and recessed windows can reduce this scattering, although in all cases we must also use wavelength filters inside the spectrometers. As this stray light is not undergoing the Doppler shifting effect of the Thomson scattered light, these filters have high rejection in and around the laser wavelength which cut out the stray light but leave the Thomson scattering spectra relatively untouched.

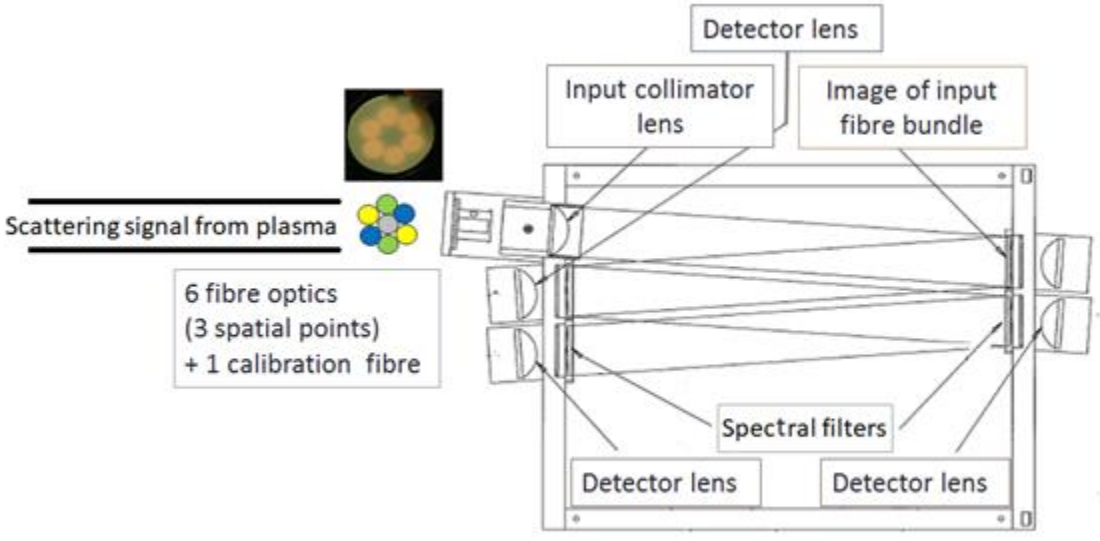

Figure 13. A 4 channel spectral polychromator of RFX-mod. Scattering signal from three spatial points are fed via a bundle of 6 fibre optics into the polychromator, which has 4 detector lenses behind 4 different spectral filters to give 4 spectral channel output.

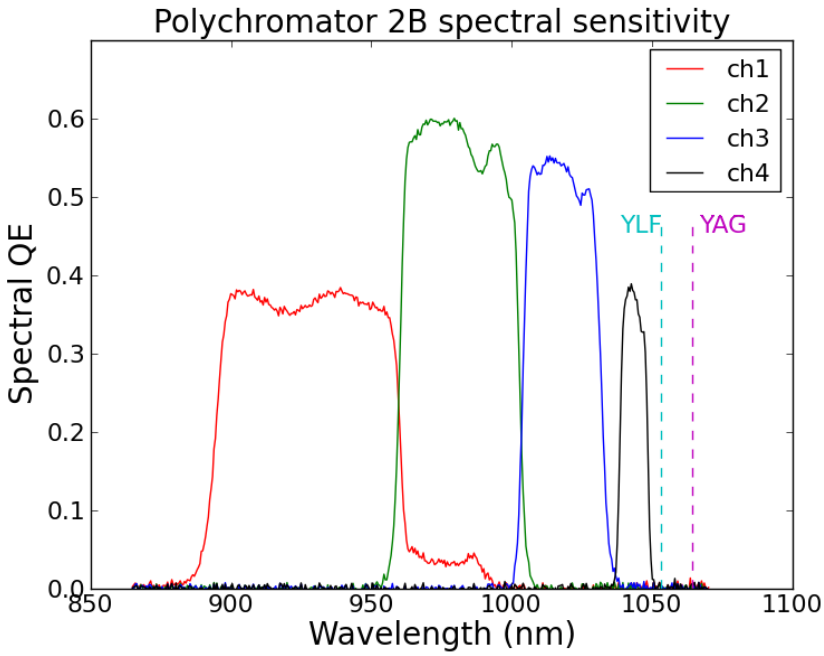

Figure 14. Transmission curves of a RFX-mod spectrometer's spectral filter channels, designed to have rejection at the Nd:YLF and Nd:YAG laser lines.

Another source of noise is plasma radiation and particularly spectral line emission. The line radiation can be rejected in the same way as the laser line, while the plasma radiation can be considered as a background level which can be subtracted from the signal, thus only fluctuations in the plasma light and not the total power is what causes signal noise, although usually at an acceptable level.

The ruby laser was the first type of laser used for incoherent Thomson scattering since it became available in the 1960's, due to its high power, high energy, and good beam quality. Its wavelength of 694.3nm also matches well with standard sensitive detector wavelengths, and ruby lasers are still used today as a well proven and standard system for these reasons. The major limiting factor of the ruby laser is its low repetition capability (up to about 1Hz). Subsequent advances in laser technology have produced the now primarily used neodymium lasers, particularly when yttrium aluminium garnet (Nd:YAG) is employed as the solid state laser medium. The major advantage of these lasers over the ruby is the ability to fire rapidly at up to 100Hz, which enables high resolution temporal evolution of the electron temperature and density.

2.4 Dual-Laser Thomson scattering

Thomson scattering (TS) systems require an initial calibration of the polychromator spectral sensitivities, which is done by illuminating the entire collection optics system with a broadband light source inserted into the vacuum chamber to obtain a set of calibration coefficients C_i^p for each spectrometer over all spectral channels. A challenge of this is that regular recalibration is required as these sensitivities may change over time. This is especially true for large machines such as ITER, where the sensitivities of optical components exposed to a nuclear environment may change more rapidly and access for recalibration requires remote handling and inconvenient shut down. Therefore a self-calibrating TS technique that can continuously produce updated correction factors as the original calibration coefficients change is highly desirable [28].

Self-calibrating TS is a technique for measuring the relative calibration coefficients of the polychromator spectral channels sensitivity C_i, based on analysing two different spectra scattered by the same plasma volume at the same time [29]. This ensures that both spectra refer to the same electron temperature T_e and density n_e. The two spectra must be distinguishable, for example having different scattering angles or different incident wavelengths. In this way, two unique spectra are produced from the same T_e and n_e. If the original sensitivity coefficients C_i are still accurate, then the fit of both spectra will give the same T_e. If the temperatures differ however, then the original C_i is no longer valid and must be adjusted with a set of correction factors CF_i to make the two spectra agree. Two main methods have been proposed for producing these two simultaneous spectra: the dual-laser method and the dual-angle method.

The dual-angle method uses a single laser where the scattering volume is observed through two different scattering angles as shown in Figure 15. The same temperature and density volume thus produces two unique spectra with different scattering angles. The dual-angle technique has been experimentally investigated [30-33], but so far is limited in accuracy due to the very small difference in the scattered spectra. It is also not practical to obtain two scattering angles over all the standard scattering volumes.

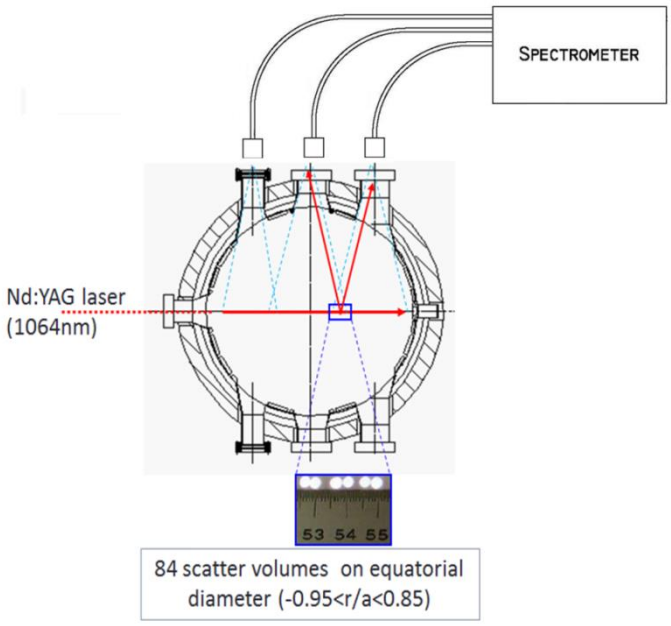

Figure 15. Simple schematic of RFX-mod multiple-angle Thomson scattering setup.

The dual-laser calibration technique investigated in this thesis [34] uses two lasers of different wavelengths, in our case the available Nd:YAG (λ = 1064nm) laser and Nd:YLF (λ = 1053nm) laser. These lasers are combined on the same path with the same polarization, and fire in synchronisation so that they can be said to pass through the same plasma volume. The two scattered spectra are observed through the same angle, but they are unique due to their different laser wavelengths. The laser wavelengths ideally should be chosen so that they are close enough for their scattered spectra to overlap, but far apart enough so that the difference between the two spectra is accurately measureable.

From [34], let NM_i and NC_i be the main (M) and the calibration (C) laser TS signals respectively, in photoelectrons, detected from the same plasma volume in the i-th detection spectral channel of the polychromator. The expected values of these signals are $NM_i = A_M C_i SM_i$ and $NC_i = A_C C_i SC_i$:

$$A_M = n_e(E_M/h\nu_M)(d\sigma/d\Omega)TL\Delta\Omega \quad \textbf{(25)}$$

$$SM_i = \int_0^\infty f_i(\lambda) n_i(\lambda) P(T_e, \theta, \lambda_M, \lambda) d\lambda \quad \textbf{(26)}$$

with similar equations for the calibration laser A_C and SC_i. E_M is the energy of the main laser pulse, hv_M is the energy of the incident photons from the main laser, T is the transmission of the collection optics, L is the length of the scattering volume, $d\sigma/d\Omega$ is the TS differential cross section, $\eta_i(\lambda)$ is the spectral quantum efficiency (QE) of the i-th detector, $\Delta\Omega$ is the solid angle of the collection optics, $f_i(\lambda)$ is the transmission function of the i-th spectral channel, and $P(T_e, \theta, \lambda_M, \lambda)$ is the spectral density function of the scattered photons [24] where λ is the detection wavelength and λ_M is the laser wavelength (in this case the main laser). The method for analysis is based on taking the data from both spectra together into a χ^2 function and minimizing it [34]:

$$\chi^2 = \sum_{i=1}^{N} \left[\frac{1}{\sigma_{M,i}^2} (NM_i - A_M C_i SM_i)^2 + \frac{1}{\sigma_{C,i}^2} (NC_i - A_C C_i SC_i)^2 \right] \quad \textbf{(27)}$$

Where $\sigma_{M,i}^2$ and $\sigma_{C,i}^2$ are the variances of the measured signals NM_i and NC_i respectively. These are calculated from the noise due to the stray light, the background plasma light and photoelectron statistics. To carry out the minimization we define $\gamma = A_M/A_C$. In an ideal case when the main and calibration lasers are well aligned along the same path through the plasma volume, we can say $\gamma = \lambda_M E_M/\lambda_C E_C$ which is simply the ratio of the number of incident photons of the main and calibration laser pulses. Practical alignments are rarely ideal however so this γ term also describes any difference in the signal due to small differences in alignment between the two laser beams, and so must be determined from the data. In this case the χ^2 becomes a function of T_e, the unknown γ, and the values $A_C C_i$, which are all determined at the same time with a N+2 parameter minimisation [34]:

$$\chi^2 = \sum_{i=1}^{N} \left[\frac{1}{\sigma_{M,i}^2} (NM_i - \gamma A_C C_i SM_i)^2 + \frac{1}{\sigma_{C,i}^2} (NC_i - A_C C_i SC_i)^2 \right] \quad \textbf{(28)}$$

The expected signals from $A_C C_i$ have a linear dependence, and so the χ^2 minimisation with respect to them is easily evaluated by solving the N equations [34]:

$$\frac{\partial \chi^2}{\partial C_i} = -2\left[\frac{1}{\sigma_{M,i}^2}(NM_i - \gamma A_C C_i SM_i)(\gamma A_C SM_i) + \frac{1}{\sigma_{C,i}^2}(NC_i - A_C C_i SC_i)(A_C SC_i)\right] = 0 \quad (29)$$

giving an expression for $A_C C_i$:

$$A_C C_i = \left(\gamma \frac{NM_i SM_i}{\sigma_{M,i}^2} + \frac{NC_i SC_i}{\sigma_{C,i}^2}\right) \Big/ \left(\gamma^2 \frac{{SM_i}^2}{\sigma_{M,i}^2} + \frac{{SC_i}^2}{\sigma_{C,i}^2}\right) \quad (30)$$

This value is substituted back into equation (28) which then becomes an easier two-parameter χ^2 minimisation of T_e and γ, solved by a two-dimensional numerical search. This dual-fit determines a single $T_e$and γ from the two sets of TS signals, given by the two different lasers. The values of $A_C C_i$ are found by substituting $T_e$and γ back into equation (30). These spectral sensitivities are generally compared to the original calibration coefficients C_i^p to produce a set of correction factors CF_i which are applied to the C_i^p coefficients. These correction factors can be recalculated at any time to keep the coefficients accurate and up to date [34].

2.5 Polarimetric Thomson scattering

The second advanced TS technique presented in this thesis is polarimetric Thomson scattering. In contrast with conventional TS which determines T_e based on the Doppler broadening of the scattered spectra, polarimetric TS is based on the depolarization of Thomson scattering radiation. The amount of depolarization is directly proportional to the electron temperature, and so the depolarized signal and thus signal-to-noise ratio increases and the technique becomes more accurate in very hot plasmas [35]. This technique is of interest for ITER where the high temperatures (40keV) make the technique competitive in accuracy with conventional TS for determining T_e. From Figure 16 we can see this depolarization has a negligible effect on the shape of the TS spectrum for the purposes of T_e measurements, however it does reduce the number of polarized

scattered photons in the observation direction. This can be up to a 20% reduction at 40keV which must be taken into account for electron density measurements [36].

Let's recall equation (15) from section 2.2.3, the scattered power per unit solid angle per unit angular frequency given by:

$$\frac{d^2P}{d\Omega_s d\omega_s} = r_e^2 \int_{vol} \langle S_i \rangle n_e d^3\mathbf{r} \int_{vel} \left(\frac{\omega_s}{\omega_i}\right)^2 \times \left\{1 - \frac{\beta_e^2\left(1 - \hat{\mathbf{s}} \cdot \hat{\mathbf{i}}\right)}{(1-\beta_i)(1-\beta_s)}\right\}^2 (1-\beta^2) \times f(\boldsymbol{\beta})\delta(\mathbf{k}\cdot\mathbf{v} - \omega) d^3\boldsymbol{\beta} \quad \textbf{(15)}$$

The term $\beta_e^2\left(1 - \hat{\mathbf{s}} \cdot \hat{\mathbf{i}}\right)/(1-\beta_i)(1-\beta_s)$ describes the depolarization of the scattered radiation. It is dependent on $\beta_e^2 = (\mathbf{v}\cdot\hat{\mathbf{e}}/\mathrm{c})^{\mathbf{2}}$, so we see that it is a relativistic effect which only becomes significant at very high electron velocities/temperatures.

The depolarization effect can be described as a change in orientation of the $\mathbf{E}_i$ field in respect to the electron rest frame, with a fraction β_e^2 of the scattered light $\mathbf{E}_s$ appearing in the orthogonal direction [25]. In other words, $\mathbf{E}_s$ has a component dependent on β_e^2, which is different for each scattering electron. The incoherent summation over all the scattering volume of these individual components produces unpolarized radiation [37]. Therefore, in high temperature plasmas, the TS radiation can be described as composed of an incoherent sum of a completely polarised component and an unpolarized component. In this manner we can write the Stokes vector S of the scattering radiation as [37,38]

$$S = \begin{pmatrix} S_0 \\ S_1 \\ S_2 \\ S_3 \end{pmatrix} = KS_0^i \left[C_{PL} \begin{pmatrix} 1 \\ S_1 \\ S_2 \\ S_3 \end{pmatrix} + C_{NP} \begin{pmatrix} 1 \\ 0 \\ 0 \\ 0 \end{pmatrix} \right] \quad \textbf{(31)}$$

Here S_1, S_2, and S_3 represent the scattered radiation, and the two matrices in the square brackets are unit Stokes vectors representing completely polarized and unpolarized light

respectively. The degree of polarization P is related to the coefficients C_{PL} and C_{NP} which are proportional to the intensities of the two components, where $P = C_{PL}/(C_{PL} + C_{NP})$. S_0^i is the first element of the Stokes vector of the incident wave and K is a normalization constant. $D = 1 - P$ is the so called "depolarization" term [39], which is a representation of the term $\beta_e^2(1 - \hat{\mathbf{s}} \cdot \hat{\mathbf{i}})/(1 - \beta_i)(1 - \beta_s)$ from equation (15). The polarization state of the frequency integrated Thomson scattering radiation can be described by a Stokes vector given by [37]

$$S(\theta, T_e) = M(\theta, T_e) \cdot S_{IN} \quad \textbf{(32)}$$

Where θ is the scattering angle, S_{IN} is the Stokes vector of the incident radiation, and $M(\theta, T_e)$ is the Thomson scattering Mueller matrix [40]. This expression will be the basis of the simple depolarization model employed in the experiment described in chapter 4.

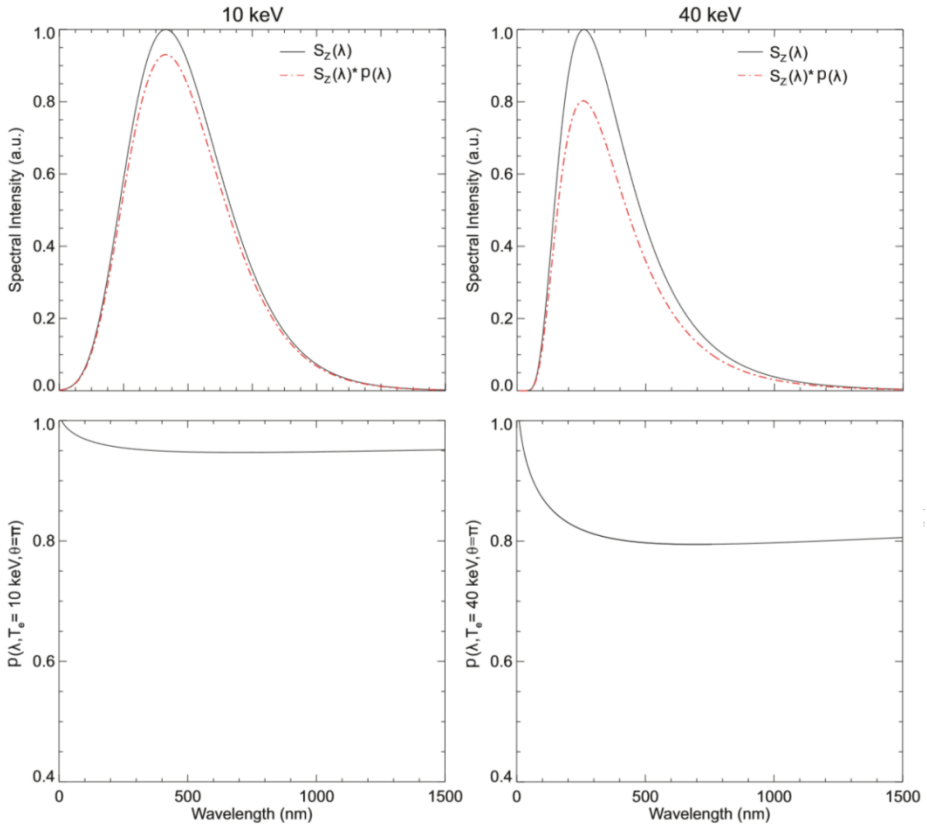

Figure 16. Depolarization effect for a laser with $\boldsymbol{\lambda = 694.3nm}$ and scattering angle $\boldsymbol{\theta = \pi}$ **[36]**. $\boldsymbol{S_z}$ is the scattered spectrum ignoring depolarization effects and $\boldsymbol{S_z * P}$ includes the degree of polarization.

CHAPTER 3: DUAL-LASER THOMSON SCATTERING IN RFX

This chapter describes the dual-laser Thomson scattering (TS) experiment undertaken in the reverse field pinch (RFX-mod) device in Padova during the first year of the doctoral studies; the results presented here are based on the published journal article written as first author [34].

Conventional TS uses a single incident laser, whose light is scattered by the plasma and observed in a polychromator spectrometer. This optical system for observing the light must first be calibrated by using a broadband light source inserted into the chamber. However, these calibration coefficients may change over time, requiring invasive recalibration. Dual-laser TS is a method for achieving self-calibrating Thomson scattering. By comparing the scattering spectra of two different lasers fired in sync to scatter from the same plasma volume, the plasma itself is used as the calibrating light source. This technique could provide continuous updating of the calibration coefficients, avoiding the obtrusive traditional recalibration method that is difficult to perform in large machines such as ITER. In what follows we outline the practical implementation of the dual-laser method on RFX-mod using the available Nd:YAG (λ = 1064nm) laser and a Nd:YLF (λ = 1053nm) laser. We also describe an analysis of the dual-laser measurements taken and present and discuss the results for a specific polychromator in a central region of the plasma. Finally, we discuss the implications of this experiment on the effectiveness of the dual-laser technique for implementation on other fusion devices.

The personal work undertaken for this dual-laser experiment included creating an optical system to combine the two available lasers together on the same path. This encompassed everything from optical design and procurement, to installation and testing. The majority of work time however was in post-experiment analysis, where the computer code for analysing the conventional TS spectra was studied and adapted to perform the dual-laser analysis. To the authors' knowledge, this is the first successful demonstration of the dual-laser technique.

3.1 Self-calibrating Thomson scattering

In section 2.4 we discussed self-calibration for a Thomson scattering (TS) diagnostic system as a technique for measuring the relative calibration coefficients of the polychromator spectral channels sensitivity *Ci*, without the need for obtrusive traditional recalibration. The technique is based on analysing two different spectra scattered by the same plasma volume. Exploiting the same plasma volume means that the electron temperature *Te* and the electron density *ne* can be considered constant for both spectra and therefore can be determined simultaneously along with *Ci*. After initial calibration of the systems' spectral sensitivities, regular recalibration is required as these sensitivities change over time due to device operation. In the self-calibrating technique, the plasma itself is used as the calibrating light source. This makes for discreet measurements that don't affect machine operation, which is very desirable for fusion devices such as ITER where access for traditional recalibration using a broadband light source requires remote handling and operational shut-down [28,41].

One variant of the self-calibration technique is the dual-angle method, which uses a single laser that is observed under two different scattering angles as described in section 2.4. The variant under investigation here is the dual-laser method which uses two lasers with different wavelength fired in sync on the same path. The time delay between the lasers is short enough (<20μm) that they can be considered to scatter off the same plasma volume, producing the two spectra to be compared. The application of the dual-laser technique to ITER and other devices has been investigated [28,42-44], but never before tested experimentally.

3.2 RFX-mod Thomson scattering system

The RFX-mod Thomson scattering (TS) diagnostic is a conventional TS system with 90° scattering. Figure 17 shows the system schematic: the incident laser has horizontal orientation with the scattering signal collected through three vertical observation ports. These ports are connected by multiplexing fibre optic lines which couple the plasma to

the 28 filter polychomators with Si avalanche photodiode (APD) detectors [45]. Each fibre optic contains three different fibre lengths to introduce two time delays of 70ns between the three lengths. Therefore each polychromator can measure the scattering spectra from three different plasma volumes. This gives a total of 84 scattering volumes across the equatorial diameter ($-0.95 < r/a < 0.85$).

Figure 18 shows the four-channel spectral configuration in the RFX-mod polychromators, of which there are two different configurations as shown. Both bandpass configurations were designed so that there is no spectral overlap of the filters with the laser lines, which is essential to the experiment to avoid pollution from the laser light. The Nd:YLF was the primary laser for TS measurements in RFX-mod but has been recently replaced by the new Nd:YAG laser system. An investigation was carried out to determine if in RFX-mod it is possible to utilize these to lasers for a dual-angle self-calibration experiment. It was found that in spite of the small difference between the laser wavelengths ($\Delta\lambda = 11$nm) that a reliable calibration should be possible with the analysis of a reasonable number of laser pulse pairs [28]. Note that in RFX-mod we also have available a ruby laser ($\lambda = 694.3$nm) and a second harmonic Nd:YAG laser ($\lambda = 532$nm) to use as a calibration laser, but this is restricted by the typical operational temperature of the device (< 1keV). At this relatively low temperature these wavelengths would be too far away from the main laser (Nd:YAG, $\lambda = 1064$nm), and would not have the necessary overlap for the calibration method to work. Either the plasma would need to be hotter to broaden the spectra more, or the wavelengths need to be closer. This left the non-ideal Nd:YAG/ Nd:YLF combination as the only useable choice available.

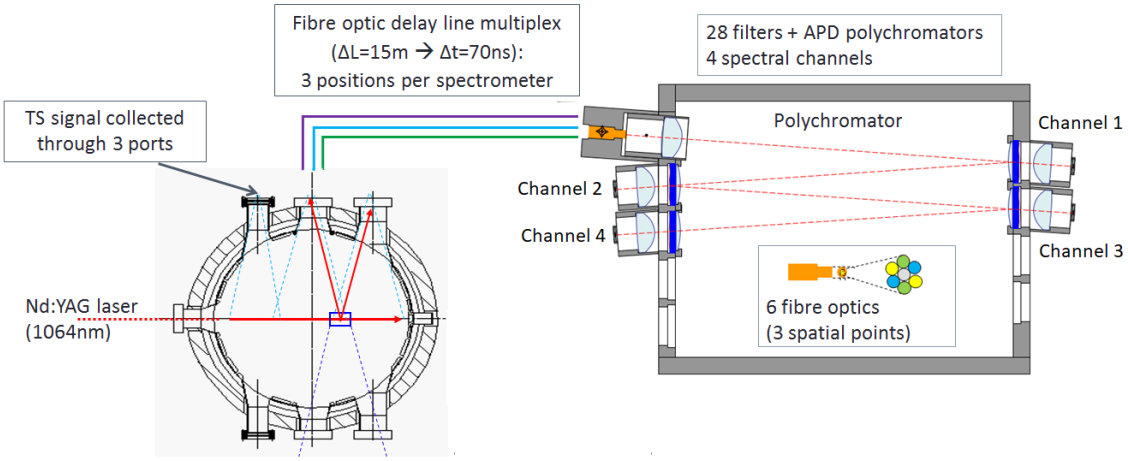

Figure 17 A schematic of the RFX-mod multipoint conventional TS system.

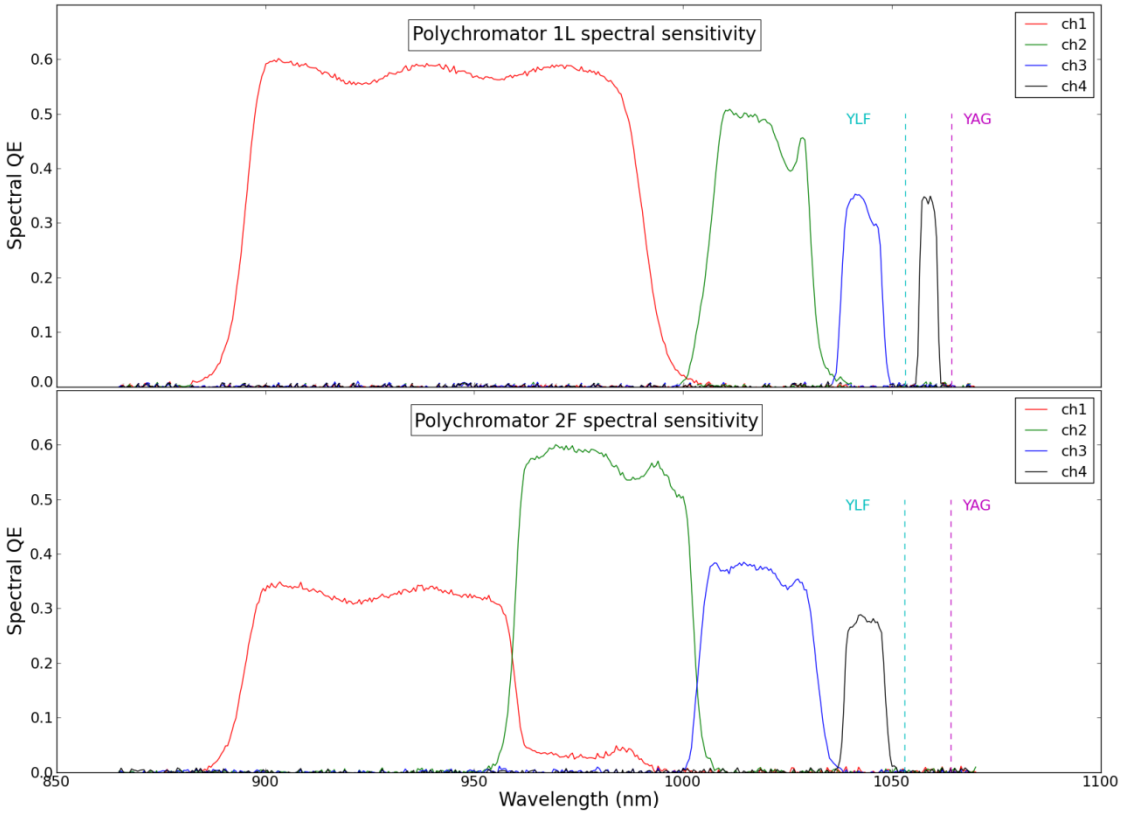

Figure 18 The spectral sensitivity of the two sets of spectral channels in the filter polychromators of RFX-mod, labelled 1L (Left) and 2F (Right). 10 of the polychromators have the 1L configuration: a large first spectral channel (red) and the fourth spectral

channel (black) between the two laser wavelengths. The rest of the polychromators have no spectral channel between the lasers as in the 2F above. See Table 1 for wavelength parameters.

Channel	Central λ (nm)	FWHM (nm)	Channel	Central λ (nm)	FWHM (nm)
1L - 1	942.2	95.5	2F - 1	929.1	65.0
1L - 2	1017.9	25.0	2F - 2	980.8	42.5
1L - 3	1042.2	9.5	2F - 3	1017.8	28.0
1L - 4	1057.6	4.5	2F - 4	1043.9	9.5

Table 1 The parameters of the spectral channels of polychromators 1L and 2F.

3.3 Laser beam combination

The main practical challenge was to combine the Nd:YLF laser along the same path and with the same polarization as the Nd:YAG laser. Normally with well-spaced wavelengths the combination of two lasers can easily be achieved by using standard wavelength selective optical components. In our case however there is only a difference of 11nm between the laser wavelengths and so this approach was not feasible. We therefore created a solution utilising the differences in the laser polarisation orientations to combine them together. This required the design, procurement, and assembly of a beam combiner, the schematic of which is shown in Figure 19. A polarising beam splitter cube (BS1) is used in reverse to first combine both lasers, followed by polarisation rotation using a dual wavelength waveplate (WP) designed to retard by λ/2 at 1053nm and by λ at 1064nm. This resulted in both beams arriving on the same path with the same polarization orientation. The second cube (BS2) is used to clean the polarisation. Burn paper images in on Figure 20 show both lasers directly before and after passing through the beam combiner. While there was minimal energy loss in the Nd:YAG when passing

through combiner, there was a ~10% reduction in energy of the Nd:YLF due to polarization losses. This was due to the Nd:YLF beam not being completely horizontally polarized as it enters the combiner.

From the burn paper images we can also see that the spatial quality and shape of the two laser beams are very different. The Nd:YAG produces a ~20mm diameter, round cross section which is quite smooth and clean from hot spots due to its two stage amplifier with two single-pass cylindrical rods. The older Nd:YLF instead employs a large slab amplifier with a zig-zag, multiple internal reflection path, which produces a ~40mm diameter, almost square cross section with a typical multimode structure featuring several hot spots. This was an additional complication as the beam combiner was comprised of all 1 inch (25.4mm) circular optical components, with a clear aperture size of about 22mm. This was acceptable for the Nd:YAG beam, however the Nd:YLF would need to be reduced. To address this we designed and applied a beam reducer to the Nd:YLF laser in the form of a simple Galilean telescope; a convex lens followed by a concave lens, shown in Fig. 4. A plano-convex/plano-concave design was selected to reduce back reflections of the laser. The beam must be slightly convergent after reduction so that it focuses inside the plasma (~9 metres after second lens). The lens equation for the beam reducer is:

$$s_2" = \frac{f_e(f_o - d)}{f_o + f_e - d} \quad \textbf{(33)}$$

We chose to use stock lenses with $f_o(\lambda = 1064\text{nm}) = 1145.6\text{mm}$ the focal length of the converging objective lens, $f_e(\lambda = 1064\text{nm}) = -572.7\text{mm}$ the focal length of the diverging eye-piece lens, $s_2" = 9000\text{mm}$ as the distance from the secondary principal point of the second element to the final combination focal point, and d as the distance between the lenses. Using these focal lengths we find that d should be ~607mm to both reduce the beam from 40mm down to ~20mm, and for it to focus inside the plasma. This was followed by the physical alignment of both lasers to be focused into the plasma after combination. Testing of the setup showed The Nd:YAG was relatively unaffected by the beam combiner and could remain online as the primary laser used in regular operation in

the RFX-mod conventional TS system. The older Nd:YLF laser operated acceptably, however it was found to produce considerable stray light particularly in the spectral channels closest to the laser line (1053nm), which did affect the signal-to-noise level for the duration of the campaign. All optical components of the beam combiner were chosen with a high laser damage threshold, however after the campaign there was minor damage to the BS1 cube. This was likely caused by the Nd:YLF beam due to the concentration of the beam size combined with the tendency for hot spots in the cross section. While the damage was too minor to affect our experiment, this type of energy density damage would need to be tackled for systems that would have prolonged operation.

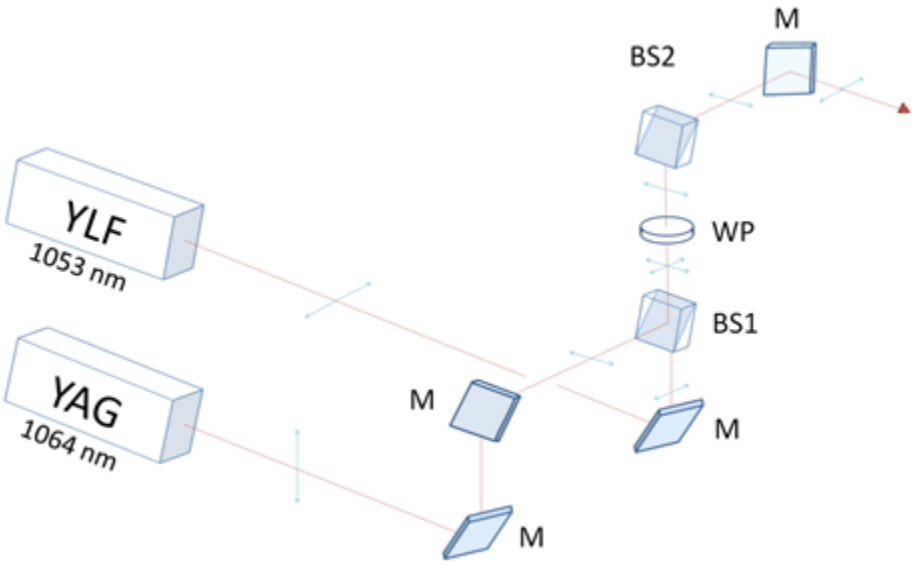

Figure 19. A schematic of the dual beam combiner, designed and implemented for the Nd:YAG and Nd:YLF lasers, consisting of two polarizing beam splitting cubes (BS1, BS2), a dual wavelength waveplate (WP), and several steering mirrors (M).

Figure 20. Burn paper images of both laser beams directly before and after passing through the beam combiner.

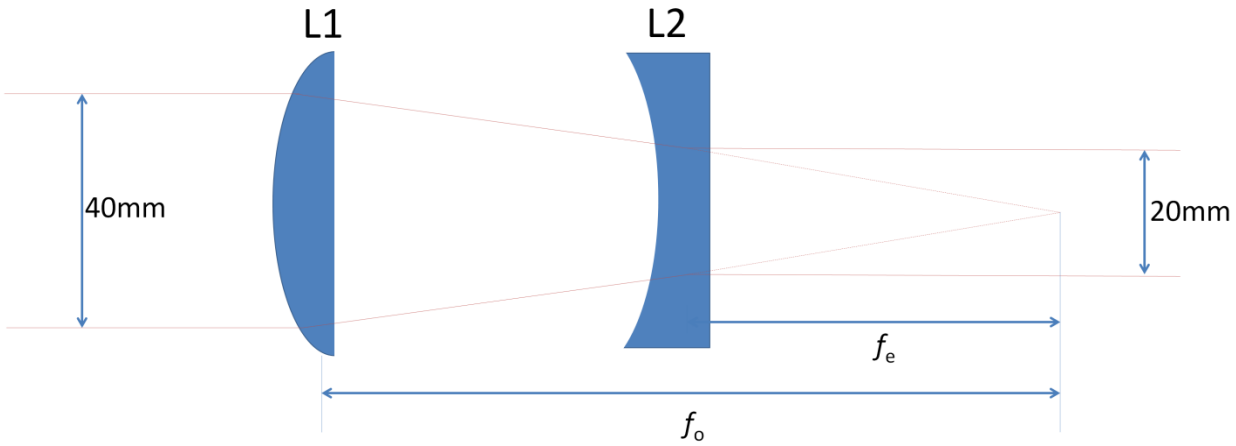

Figure 21. A schematic of the designed and implemented Nd:YLF beam reducer, consisting of a plano-convex objective lens (L1) and plano-concave eye-piece lens (L2), Shown is the requirement for a parallel output; for a convergent beam the distance between the lenses should be slightly larger than $f_o + f_e$ as per equation (33).

3.4 Laser synchronisation

A further challenge was the laser timing and synchronization, to ensure that the Nd:YLF and Nd:YAG were fired together with a delay short enough that both lasers can be said to pass through the same plasma volume with the same T_e and n_e. The Nd:YLF laser has very precise firing times as it is actively Q-switched. The Nd:YAG however is passively Q-switched, which results in microsecond scale jittering in the firing times. On top of this there are different internal delays for each laser, 30ms for the Nd:YAG and 5.2ms for the Nd:YLF. In the end, precise timing was achieved by using an oscilloscope and a delay generator to synchronize both lasers to fire within a few microseconds.

The laser bursts are fired using the same initial single trigger. However these bursts last for the duration of the plasma discharge, and each subsequent pulse after the initial trigger is fired via the different internal clocks of the two lasers. Although the initial triggering was accurate, the drift caused by the disparity of the internal clocks didn't allow for precise pulse pairing across the entire plasma discharge. For considering a YAG/YLF pulse pair suitable for the dual-laser analysis, a maximum delay between the lasers of 20μs was chosen as acceptable to ensure we can consider T_e and n_e constant. 20μs is a reasonable delay value considering the typical MHD timescales in the RFX plasma core are on the order of milliseconds [46].

The duration of the plasma in RFX-mod allows for around ten YLF/YAG pulse pairs per discharge. However, due to this trigger drift the number of pulse pairs with an acceptable delay was severely reduced. To maximise pulse pairs the YLF was set to trigger several tens of microseconds before the YAG and allowed to drift closer and eventually overtake the YAG trigger, so that we had a window of ±20μs around the YAG trigger to match the YLF trigger with. This resulted in obtaining about four or five acceptable pulse pairs per discharge. Note that because of this negative to positive timing drift, when any of the pulse pairs are too close together (< 1μs) this causes loss of data acquisition, as the acquisition modules are not fast enough to rearm in time.

3.5 Dual-laser spectral analysis

From Figure 17 we can see that each spectrometer measures 3 radial points along the equatorial diameter, with full coverage from -0.41m to +0.39m around the centre with about one scattering volume every 10mm. A single spectrometer contains 4 spectral channels, whose sensitivity was previously calibrated with a broad-band tungsten ribbon lamp and a monochromator. This self-calibrating technique provides a set of correction factors CF_i for monitoring the changes of the sensitivity over time, which are applied to the original calibration coefficients C_i. These correction factors are determined from the difference between the individual and the dual-laser spectra. Figure 22 shows an example of the Nd:YAG and Nd:YLF electron temperature profiles for a single pulse pair,

presenting the single fit temperatures of the two lasers with varying degrees of convergence per polychromator. Accordingly, on an individual level, some polychromators had larger useable data sets than others.

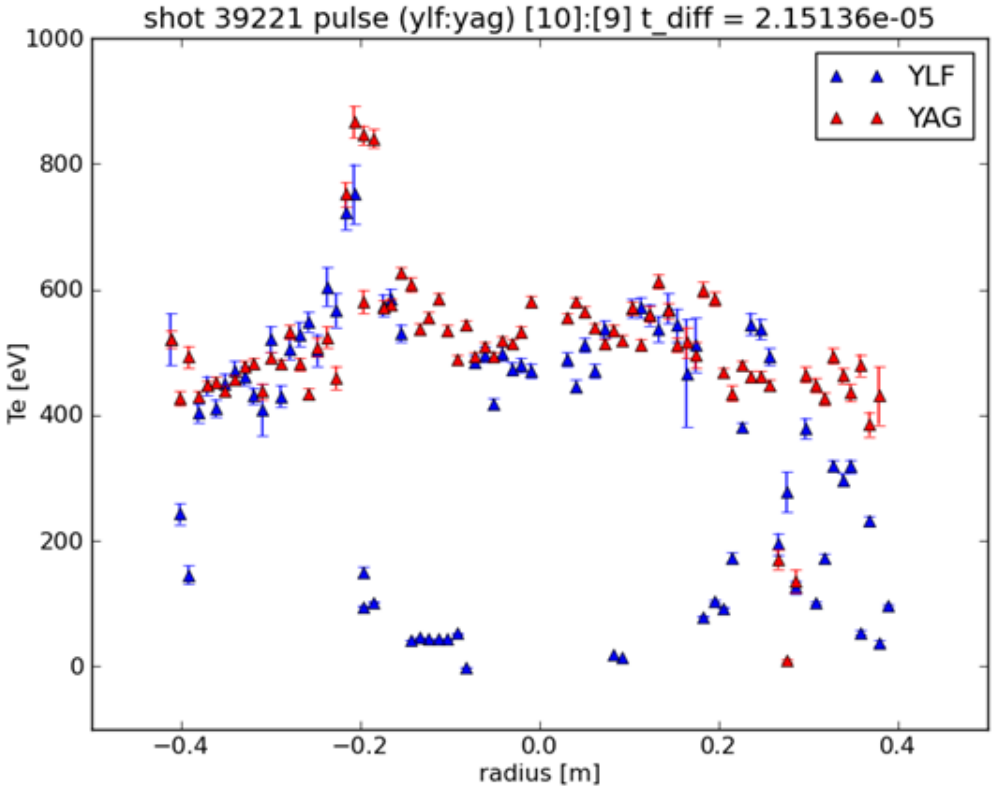

Figure 22. Sample electron temperature profile from 84 scattering volumes across the equatorial diameter of the plasma. Single fit temperatures of laser pulse pairs with varying degrees of convergence per spectrometer.

We have applied the self-calibrating method described in section 2.4 to two separate polychromators, one from each filter setup as shown in Figure 18. These polychomators, which observe different plasma regions, are labelled 2F (-0.02m to +0.03m) and 1L (+0.27m to +0.29m). It should be stated again that the dual-laser TS system set up in RFX-mod is not optimal. The use of the Nd:YAG laser ($\lambda = 1064\text{nm}$) and the Nd:YLF laser ($\lambda = 1053\text{nm}$) is the only current practical option, although the small difference in the spectra limits the sensitivity of the self-calibrating measurements. Nevertheless, reliable measurements of the calibration coefficients can be obtained with a statistical analysis of a reasonable number of laser shots with good signal to noise ratio (S/N). With

our dual-laser set up we have a dataset of ~340 self-calibration laser pulses from a campaign of ~50 plasma discharges.

For the data analysis, we first applied the conventional TS analysis method, using the standard Selden approximations described in section 2.2.4, to fit the YAG and YLF spectra separately using the original calibrations factors C_i^p [34]. This gives two independent electron temperature values T_e^{YLF} and T_e^{YAG}, as well as two quantities A_M^p and A_C^p, which correspond to two independent values of the electron density n_e^{YLF} and n_e^{YAG} in arbitrary units. Recall that if C_i^p are 100% valid then these individually fitted values from the two lasers should be the same ($T_e^{YLF} = T_e^{YAG}$ and $n_e^{YLF} = n_e^{YAG}$). However, in all measured cases there were differences in the fitted values.

We then applied our self-calibrating dual-fit technique described in section 2.4. Figure 23 shows an example of results from the analysis of two spectral pairs for both the 2F and 1L spectrometers. The values of the T_e^{YLF} and T_e^{YAG} individual fits are different as expected, and the value T_e^{dual} obtained from the dual-fit technique is quite close to the average value of the individual fits. Not all data are as nice as shown in this figure however. Stray light from the Nd:YLF greatly affects the spectral channel closest to the laser lines, while the χ^2 minimisation (equation (28)) fails to converge in many cases due to the signal noise and the closeness of the spectra. In particular, the channel centred around 1043nm in both filter setups had to be excluded from the analysis due to excessive noise. As encountered before with the dual-angle method [47], the self-calibration technique is very sensitive to measurement errors in the scattering signals. In this case, it is mainly inflicted by the suboptimal closeness of the available laser wavelengths, which provide for very small differences in the two different spectra produced. The difference between the spectra is in a lot of cases less than the typical noise. Nevertheless it was possible to perform a statistical analysis on a subset of the data determined by the same restrictions as were employed in the dual-angle experiment [47]. From [34], we restricted our analysis to the spectral pairs for which 1) both the individual best-fits converge to a pair of T_e and relative n_e values; 2) the individually fitted T_e^{YLF} and T_e^{YAG} and n_e^{YLF} and n_e^{YAG} do not differ by more than 50%; 3) the dual-spectra fit

converges to a the T_e^{dual} value which differs not more that 50% from the average value of T_e^{YLF} and T_e^{YAG}.

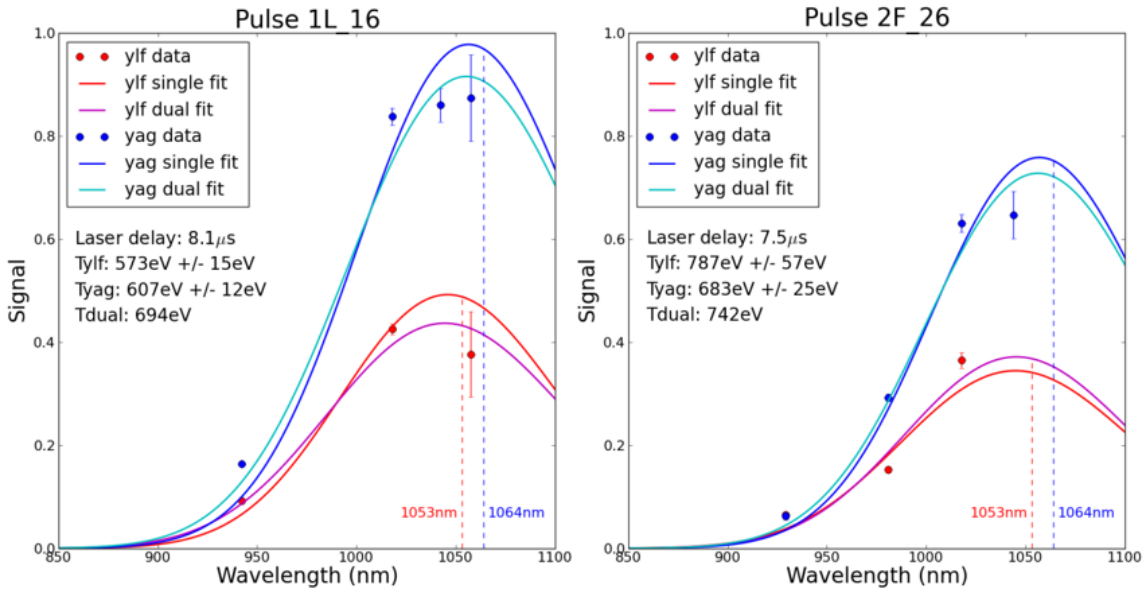

Figure 23. A comparison between the spectra fitted individually (blue and red curves) and with the dual-laser technique (cyan and purple curves) for the two sets of signal data from the Nd:YAG (blue dots) and Nd:YLF lasers (red dots). The left and right images are for independent data sets for individual laser pulse pairs observed by the 1L and 2F spectrometers respectively. The laser delay is the time delay between the Nd:YAG and Nd:YLF lasers in each pulse pair.

These criteria reduce our useable data set to ~140 laser pulses with which we can perform our statistical analysis. Figure 24 shows the correction factor for each pulse pair spectra across the four spectral channels of the 2F spectrometer. Table 2 shows the averaged values and standard deviations of the correction factors for the Nd:YAG primary laser, calculated individually for each pulse as

$$CF_i = A_M C_i SM(T_e^{dual}) / A_M^p C_i^p SM(T_e^{yag})$$

The correction factors of each spectral channel are all close to 1, which implies the original calibration coefficients C_i^p are still acceptable. Channel 1 is the channel furthest away from the laser lines and typically receives very low scattered signal, which is reflected in the significant fluctuations and large standard deviation shown. Channel 4 is particularly affected by straylight from the Nd:YLF laser as it is the channel closest to the

laser lines, which is reflected in its higher fluctuation and standard deviation than that of the central channels. Channels 2 and 3 have minimal fluctuations as they receive good levels of scattering signal and are unaffected by extra noise from being too close to the laser lines. These results show that, despite the small difference in the wavelength of the lasers scattered spectra, reliable measurements of the calibration coefficients can be obtained and the method is statistically significant.

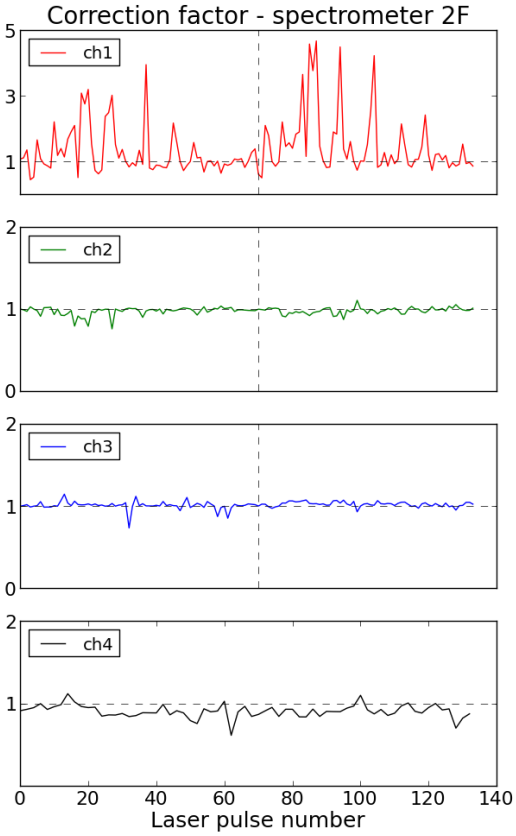

Figure 24 From **[34]**. The correction factors $\boldsymbol{CF_i}$ for the main laser in the 2F spectrometer across the four spectral channels.

Channel	*Correction factor*	*Standard deviation*
1	1.381	0.85
2	0.977	0.05
3	1.016	0.04
4	0.905	0.08

Table 2. Average values with standard deviations of the correction factors CF_i for the relative calibration coefficients C_i^p of the four spectral channels in spectrometer 2F.

3.6 Conclusions

During the first year of studies, we have carried out the testing of the dual-laser self-calibrating TS technique in RFX-mod. In our case the reliability of the technique suffers considerably from the similarity of the two laser spectra. This is the main concern and highlights the need to select of two laser systems with well separated wavelengths that produce a significant difference in the two TS spectra, while still being close enough that their spectra overlap. This selection of lasers is much easier to achieve at higher temperatures where the TS spectra will be much more spectrally stretched.

On smaller concerns, there was increased error due as lack of signal in the channel furthest from the laser lines, as well error from stray light of the system in the channel closest to the laser wavelengths. The laser timing and drift was a challenge given the different firing rates and internal clocks of the available lasers, which ultimately reduced the useable dataset by over 50%. The poorer quality of the Nd:YLF laser, combined with the need to reduce the beam size by half before entering the combiner, presented trouble regarding stray light and small damages to the combiner optics.

Despite these limitations, the dual laser combiner setup was successful, and reliable measurements of the calibration coefficients can be obtained with a statistical analysis of

a reasonable number of laser shots with a good signal-to-noise ratio. This dual-laser method could be practically applied to most fusion devices that employ Thomson scattering, and could provide continuous online monitoring of the spectral transmission of the entire detection system. This may prove essential in larger devices (ITER), where access to optical components for traditional calibration is difficult. To the authors' knowledge, this dual-laser technique has never been successfully demonstrated before.

CHAPTER 4: POLARIMETRIC THOMSON SCATTERING IN JET

This chapter describes the Polarimetric Thomson scattering experiment undertaken in the Joint European Torus (JET) device in Culham, Oxford during the second year of the doctoral studies; the results presented here are based on the journal article submitted for publishing as co-author [48].

We have measured, for the first time in a fusion plasma, the depolarization of Thomson scattering radiation. This depolarization is the basis of polarimetric Thomson scattering, an alternative to the conventional Thomson scattering (TS) technique for measuring the plasma electron temperature T_e. Polarimetric TS differs from other techniques as it relies solely on this depolarization effect, and not on the reconstruction of the Doppler broadened frequency spectrum performed in conventional and self-calibrating TS. Depolarization of the laser light is a relativistic affect and so is only applicable in high temperature plasmas (> 10keV). The degree of depolarization has an approximately linear relationship with T_e, therefore the depolarized signal gets stronger and the technique more accurate with increasing electron temperatures. The technique becomes highly competitive in accuracy with conventional TS at the high temperatures of which ITER will operate (~40keV), and could provide a supplementary independent measurement of T_e. To the author's knowledge, this is the first experiment of its kind to measure this effect and demonstrate the validity of the polarimetric TS technique.

The personal work undertaken for this experiment included onsite familiarisation with the JET High Resolution Thomson scattering (HRTS) system, modification and installation of an unused polychromator spectrometer, onsite data acquisition, and a scratch built Python code for polarimetric TS data analysis.

4.1 Polarimetric Thomson scattering

In chapter 2 we presented conventional Thomson scattering (TS) as a powerful and reliable plasma diagnostic that can provide high spatial and temporal resolution

measurements of the electron temperature and density (T_e and n_e) in a fusion plasma. This method employs an input laser which scatters off the plasma and is observed at some scattering angle by a polychromator spectrometer. From this data we reconstruct the scattered spectrum which has been Doppler broadened in the Thomson scattering process, and from the shape of the spectrum and intensity of the signal we can infer T_e and n_e respectively.

In section 2.5 we described Polarimetric TS as an alternative technique for measuring the T_e and n_e. This technique is not reliant on the Doppler broadening effect of Thomson scattering but rather on a different effect, namely the depolarization of the Thomson scattered radiation. This depolarization is a relativistic effect that has been first postulated [22] and later studied by several authors [23,39,40,49,50], who ascertained the TS radiation from very hot plasmas was partially polarized, being an incoherent sum of a completely polarized and a randomly polarized component, represented by equation (31).

The polarimetric TS technique is not been implemented before, as the depolarization effect is weak at the temperatures of present day fusion devices (< 10keV). However at higher temperatures the signal, and thus accuracy, becomes much stronger to the point of being competitive with conventional TS [35]. This is particularly true when we consider the difficulties facing conventional TS in the conditions of operation for the ITER core plasma Thomson scattering (CPTS) system, where the electron temperature will be so high that the width of the TS spectrum exceeds the limited detection spectral range of the system spectrometers (500 - 1000nm) [51]. In other words as the TS spectrum becomes increasingly stretched by higher temperatures, larger portions of the spectrum will be cut and undetectable by the measurement system, giving less measured signal and higher errors.

Figure 25 shows a comparison of the T_e and n_e measurement errors for polarimetric and conventional TS in the expected conditions of the ITER CPTS system [35]. We see here the clear increase in T_e and n_e errors for conventional TS at higher temperatures, which is very dependent on the spectral cut-off limit. For Polarimetric TS there is a sharp decrease in error above 10keV, performs better in all cases above 30keV, and is practically independent of the detector cut-off limit.

Despite clear interest in this technique, the depolarization of Thomson scattering radiation has never before been experimentally observed in a fusion plasma. In what follows we will report on the first measurements of this depolarization signal, obtained with the JET HRTS system, and the subsequent analysis and agreement with the theory.

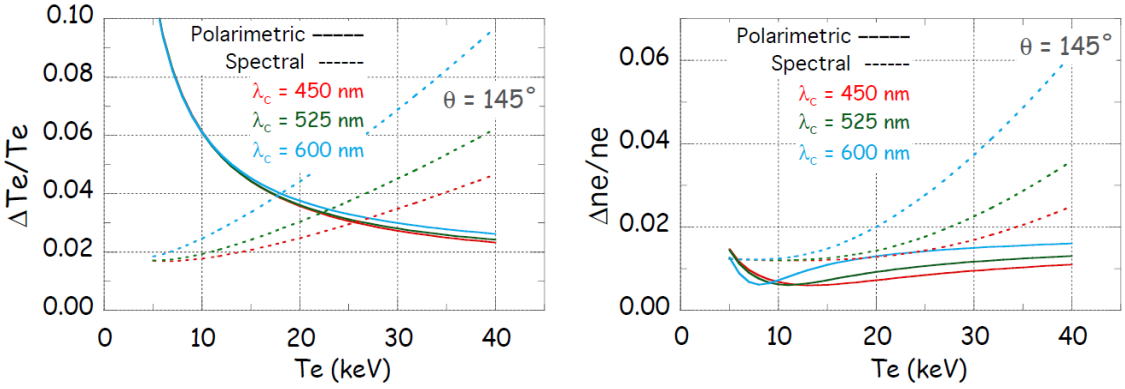

Figure 25. From [35]**.** Comparison of the T_e and n_e measurement errors for polarimetric and spectral TS in the expected conditions of the ITER core TS system.

4.2 JET HRTS system

This experiment was performed using a portion of the High Resolution Thomson Scattering (HRTS) diagnostic on the Joint European Torus (JET). The JET HRTS system has a conventional 90° scattering geometry (Figure 26) with up to 63 scattering volumes along the equatorial diameter from around the plasma centre to the outer edge (R = 2.9-3.9m), with a spatial resolution of ~15mm [52]. For reference, the typical expected plasma core is situated at around R = 3.1m (Figure 28). The system employs a 5J Nd:YAG laser ($\lambda = 1064$nm) with a repetition rate of 20Hz.

Light from these scattering volumes is collected through a vertical main upper port and imaged onto a linear array of 1mm diameter fibres. The fibres are arranged in pairs with two fibres used for each scattering volume. Three scattering volumes (6 fibres) are combined in each of the 21 filter polychromators via optical delay lines, which temporally separate the three signals to be recorded in the same 500ns data acquisition window and resolved at 1 Gs/s by transient digitizers.

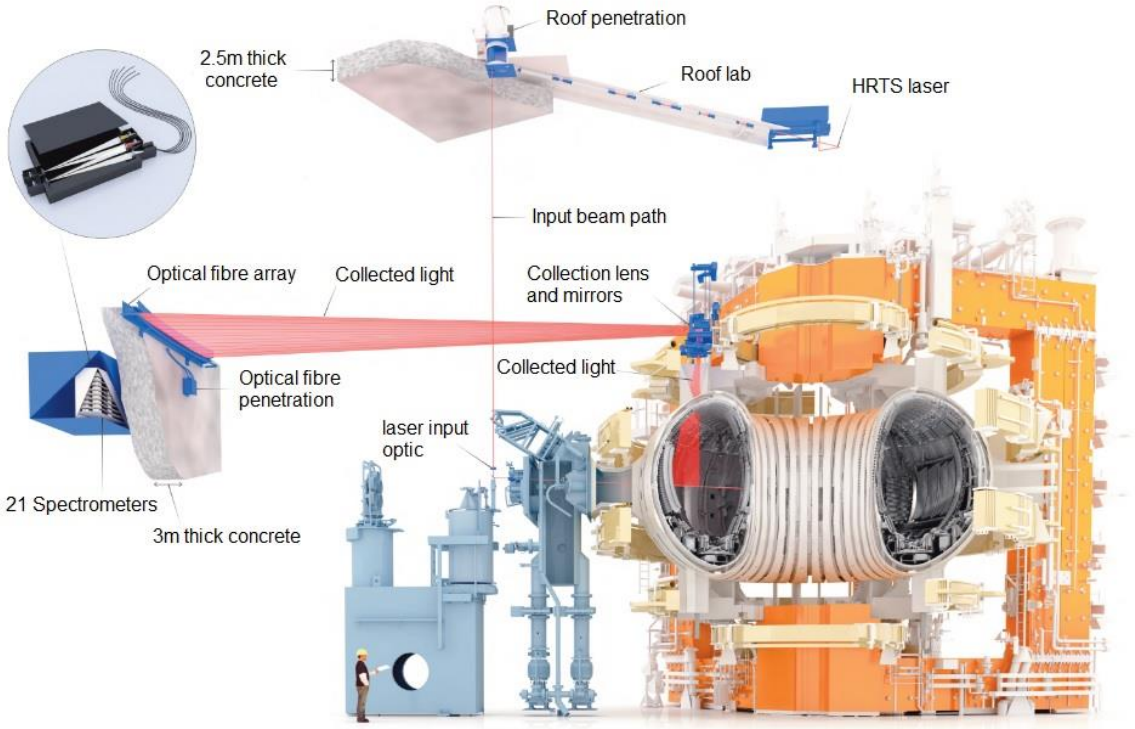

Figure 26. Schematic of the JET HRTS system set up. The scattered light is collected by the optical fibre array situated inside the torus hall.

4.3 Polarizer installation

From Figure 26 we can see the HRTS optical fibre array is situated in the torus hall. Figure 27 shows a close up of this array, where the collected light is reflected by parabolic mirrors onto the fibre optics which feed into the spectrometers. On the inner edge of the system, just the far side of the plasma core (R < 2.96m), were several installed fibres that were unused for the conventional HRTS measurements. A simple linear polarizer, with orientation perpendicular to the incoming polarization of the scattered laser light, was placed in front of the parabolic mirrors of fibres 124 and 125 (R = 2.953m). These were the unused fibres closest to the expected plasma core, to be used as the fibre pair for the polarimetric signal channel. Fibre 126 was partially covered by the polarizer, so fibres 127 and 128 (R = 2.929m) were chosen as an adjacent pair to be used as the control channel that should experience approximately the same plasma temperature and density. Figure 28 shows a cross section of the plasma, describing the

laser path and position of the selected fibres. Both sets of fibres were connected to the same polychromator, with a direct line for the polarizer fibres and a 60m delay line for the control fibres. In this way both signals can be resolved and measured with the same spectral sensitivity, and so any dependence from the polychromator parameters (quantum efficiency, spectral transmission) will cancel out in the signal ratio and can be neglected.

Figure 27. Polarizers installed on fibres 124 and 125 of JET HRTS optical fibre array.

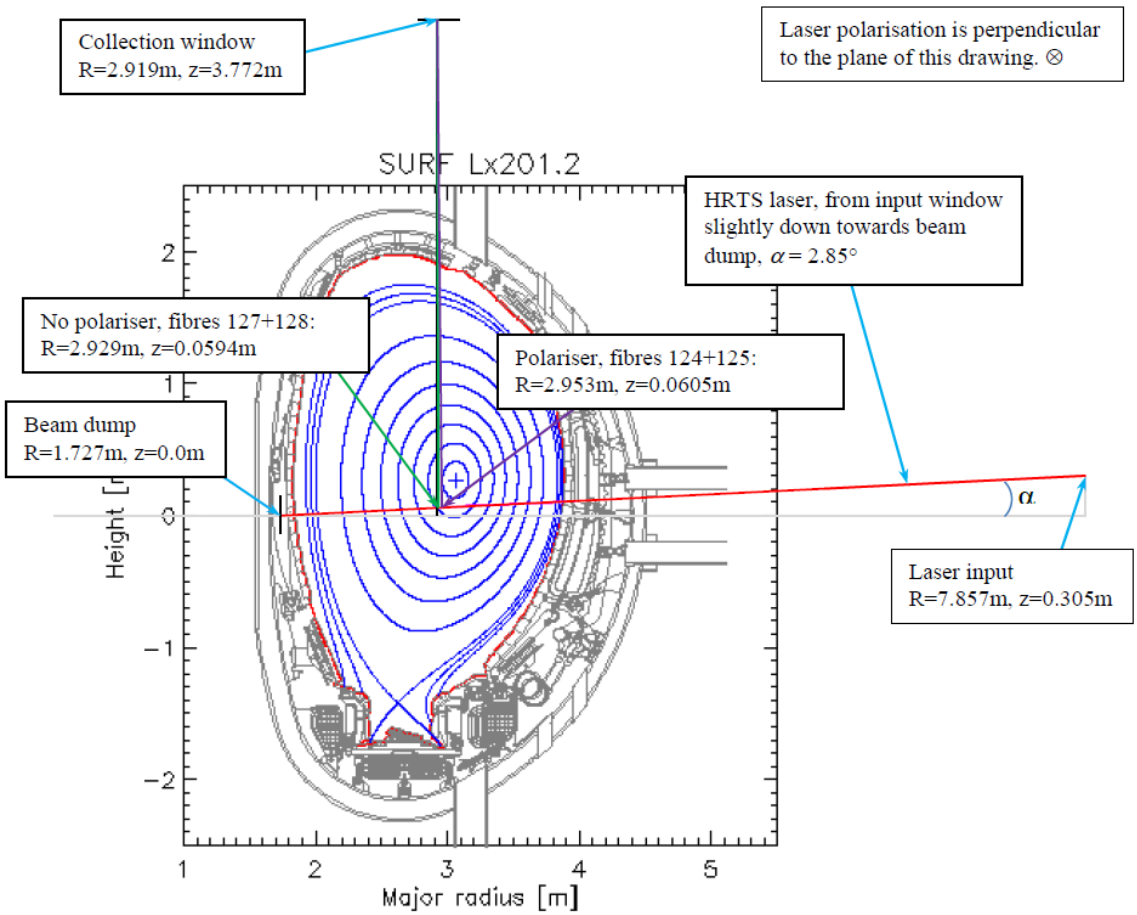

Figure 28. Cross section of the plasma, showing the laser path and position of the polarimetric and control fibres.

Figure 29. shows the schematic of a typical HRTS polychromator. A spare polychromator was available to be modified for this experiment. The standard polychromators contain four bandpass filters which give four spectral channels. However, in our depolarization experiment we are only interested in total signal, not wavelength, so to increase the sensitivity of the used polychromator, the bandpass filters were replaced with a single notch filter in Channel 1 which collects most of the scattered spectrum except around the laser line at 1064nm. As noted previously, it is possible to record three scattering volumes in the same polychromator, but for our purposes only two were required.

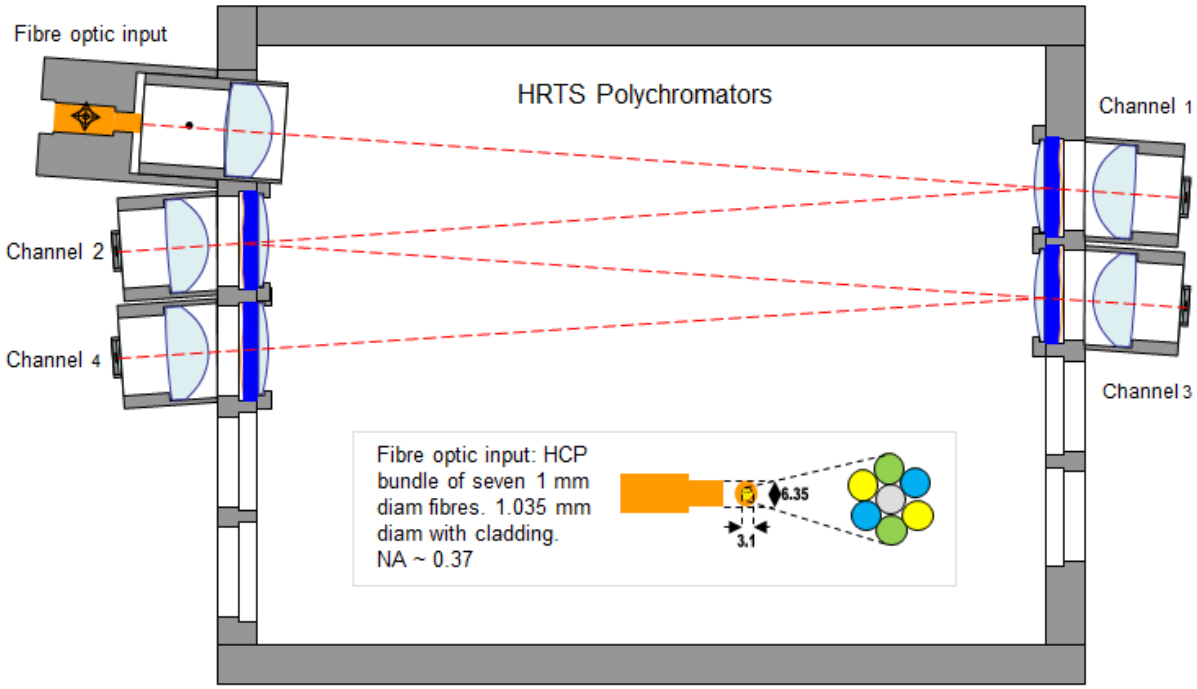

Figure 29. Schematic of the JET HRTS polychromators. In this experiment channel filters 2, 3, and 4 were removed and the channel 1 filter replaced by a laser line notch filter, to maximize signal gain while still removing the stray laser light. Only two pairs of fibres were required (polarimetric channel and control channel), rather than the usual three pairs used in the standard polychromators.

4.4 Simple depolarization model

We define I_0 and $I_\perp$ as the TS signals transmitted into the control channel and to the depolarized channel, respectively. Let $N_\perp$ and $N_\parallel$ the number of photons scattered by the plasma in the parallel and perpendicular polarization states. Due to the contrast ratio of the polarizer and to the additional depolarization effects in the collection optics and windows, the signal $I_\perp$ will collect also a small fraction k of the photons emitted in the parallel polarization. This baseline depolarization is not due to Thomson scattering, so we call k the system depolarization factor. The I_0 signal, receiving all polarizations, will be composed of $N_\parallel$ and $N_\perp$. We also need to take into account the different sensitivities of these two collection channels. Therefore the measured signals and their ratio can be written as:

$$I_{\perp} = A(N_{\perp} + kN_{\parallel}) \quad (34)$$

$$I_0 = B(N_{\perp} + N_{\parallel}) \quad (35)$$

$$\frac{I_{\perp}}{I_0} = \frac{A}{B}\left(\frac{N_{\perp} + kN_{\parallel}}{N_{\perp} + N_{\parallel}}\right) \quad (36)$$

$$\frac{I_{\perp}}{I_0} = C\frac{N_{\perp}}{N_{\perp} + N_{\parallel}} + Ck\frac{N_{\parallel}}{N_{\perp} + N_{\parallel}} \quad (37)$$

Given $N_{\perp} \ll N_{\parallel}$ we can approximate:

$$\frac{N_{\parallel}}{N_{\perp} + N_{\parallel}} \simeq \frac{N_{\parallel}}{N_{\parallel}} = 1 \quad (38)$$

Therefore:

$$\frac{I_{\perp}}{I_0} = C\frac{N_{\perp}}{N_{\perp} + N_{\parallel}} + Ck \quad (39)$$

$$\frac{I_{\perp}}{I_0} = CR(T_e) + Ck \quad (40)$$

Here $C = A/B$ is the ratio of the channel sensitivity coefficients, and the ratio $R(T_e) = N_{\perp}/(N_{\perp} + N_{\parallel})$ is a function of T_e only. In the experimental conditions of JET the two signals are detected at two different times in the same spectral channel of a JET polychromator and therefore, assuming that the transmission is the same for both, the dependence from the collection optics parameters cancels out in the ratio. Then they can be calculated to a very good approximation by using the Stokes vector $S(T_e)$ of the (frequency integrated) TS radiation which is given:

$$S(\theta, T_e) = M(\theta, T_e) \cdot S_{IN} \quad (41)$$

Here θ is the scattering angle, $M(\theta, T_e)$ is the TS Mueller matrix [40], and in our case $S_{IN} = (1,1,0,0)^T$ is a unit Stokes vector representing the incident laser radiation with

linear horizontal polarization (LHP). Given the structure of the $M(\theta, T_e)$ matrix, the last two components of $S(T_e)$ are null, while the first two components are given by [38]:

$$S_0 = M_{00} + M_{01}$$
$$S_1 = M_{01} + M_{11} \quad (42)$$

Where [40]:

$$M_{00} = 1 + u^2 - 2G(\mu)(u^2 + 4u - 3) + (16/\mu^2)(1 - \mu)^2$$
$$M_{01} = M_{10} = 1 - u^2$$
$$M_{00} = 1 + u^2 + 2G(\mu)(u^2 - 4u + 1) + (12/\mu^2)(1 - \mu)^2$$
$$u = \cos\theta \quad , \quad \mu = m_e c^2/T_e \quad , \quad G(\mu) = \frac{K_1(\mu)}{\mu K_2(\mu)}$$

Here K_1 and K_2 are modified Bessel functions of the second kind, u represents the dependence on scattering angle and $G(\mu)$ the dependence on electron temperature. The photon signals can then be written:

$$N_0 = S_0$$
$$N_\perp = \frac{1}{2}(S_0 - S_1) \quad (43)$$

and the polarization ratio for a defined scattering angle θ:

$$R(T_e) = \frac{N_\perp}{N_0} = \frac{M_{00} - M_{11}}{2M_{00} + 2M_{01}} \quad (44)$$

With this expression for $R(T_e)$ can be very well approximated by a linear dependence on T_e, giving $R(T_e) \simeq \alpha T_e$, with $\alpha = 1.872 \times 10^{-6}$ for our scattering angle of $\theta = 92.5°$ as calculated in Figure 30.

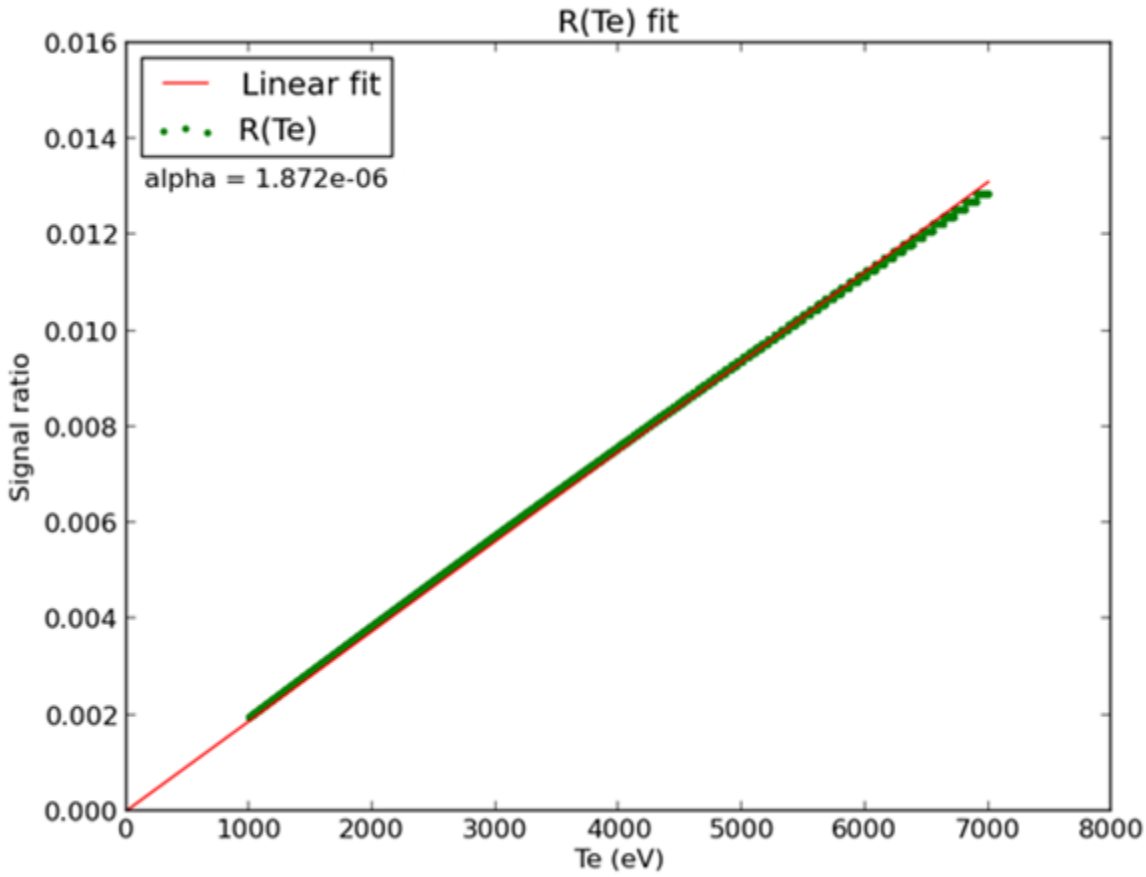

Figure 30. Plot of $R(T_e)$ at $\theta = 92°$ as a function of temperature up to 7keV, with a linear approximated slope through zero of $\alpha = 1.872 \times 10^{-6}$.

This gives equation (40) as:

$$\frac{I_\perp}{I_0} = C\alpha T_e + Ck \qquad (45)$$

This formula can be expressed as a simple line equation, of the form $I_\perp/I_0 = aT_e + b$, which we can use to perform a simple linear fit of the experimental data. From this simple fit, the slope of the line a determines $= a/\alpha$, and the intercept of the line b with the $I_\perp/I_0$ axis determines $k = b/C$.

4.5 Data analysis

The polarimetric measurements were taken during the C36B Deuterium JET campaign. This campaign produced a polarimetric data set of about 300 useable plasma pulses with core temperatures ranging from 1keV to 8keV. The depolarized signal from an individual laser pulse is lost in the noise, therefore we would have to stack up several congruent laser signals and average over them to pull the depolarized signal from the noise. Within each pulse a time window was selected to extract data only during a flat top of both T_e and n_e, ranging from 1 - 10 seconds depending on each pulse. During each flat top time window, the TS laser fires several times, with the data acquisition system being triggered each time to take measurements in 500ns data segments, timed around each laser pulse. The signal for analysis is averaged over these cumulated segments and a double Gaussian fit is applied (Figure 31), with limits on the polarimetric channel peak position to eliminate bad fits.

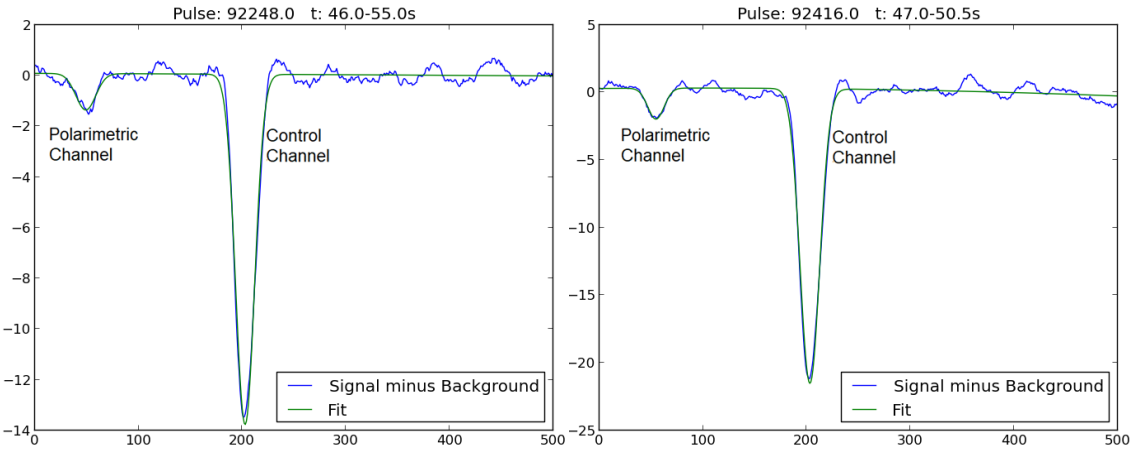

Figure 31. Two individual typical pulse signals averaged over the flat top time window minus background and stray light, showing the polarimetric $I_\perp$ and control I_0 signals.

The same respective time windows were used to calculate the average temperature T_e of each pulse during flat top. Although the four fibres cover a radial range of just over 3cm near the core of the plasma, we must assign a single average T_e to the signal ratios. The median radial position between the collection fibres is R = 2.941m which is not covered by the HRTS measurements, and so T_e was approximated as the closest recorded temperature at R = 2.9745m.

A plot of the measured signal ratio $I_{\perp}/I_0$ as a function of T_e, fitted with our simple linear function according to equation (45) , which gives $C_{Measured}$ = 5.45 ± 0.77 and k = (8.61 ± 2.37) × 10^{-3}. The measured value of C suggested that the polarimetric channel sensitivity was over 5 times higher than that of the control channel, which was surprising. It was suspected that such a difference in sensitivity may be due to a misalignment of the control channel collection optics.

In order to definitively prove that the signal we see is the TS depolarization signal, our experimental data fitted with the simple depolarisation model must give the same values of C and k as the actual optical system. As there was no time to make pre-experiment calibrations, we would need to carry out some form of post-experiment calibration to confirm the true values of C and k, and compare them with our fitted ones.

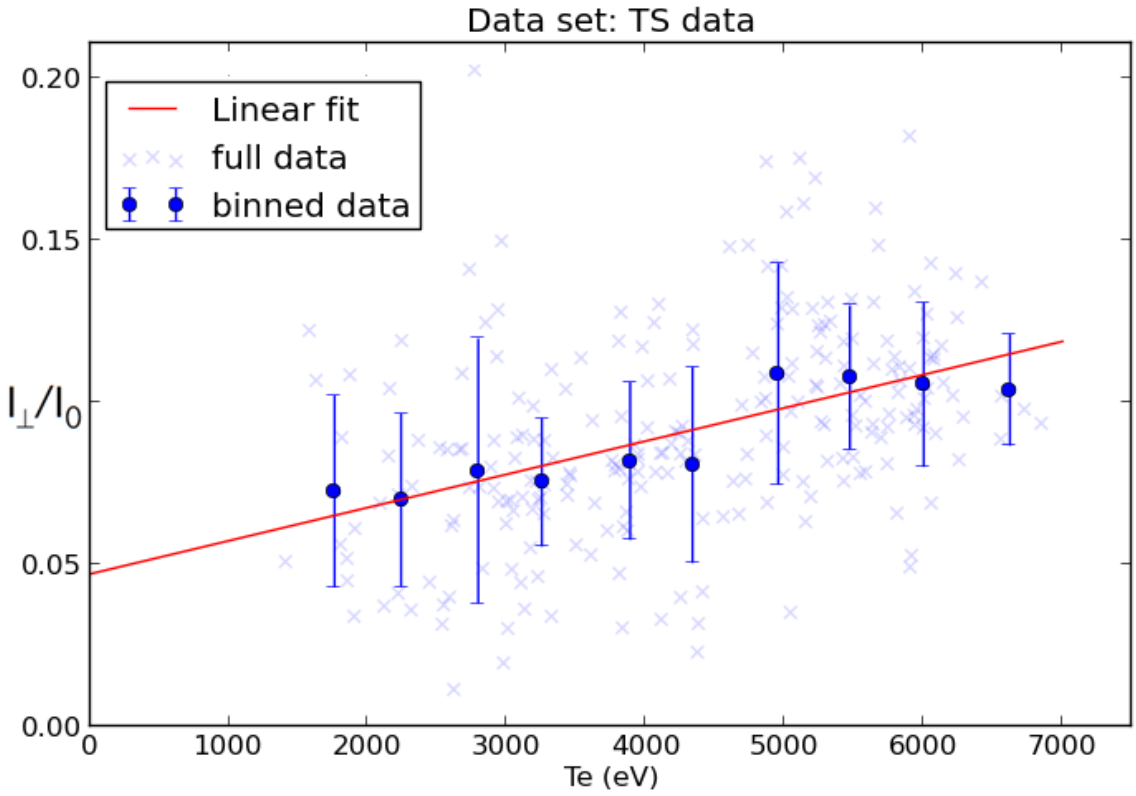

Figure 32. The measured signal ratio as a function of the plasma T_e. The parameters C and k are respectively determined from the slope and intercept by a simple, unweighted linear fit of the data points (crosses) from all 300 useable plasma pulses. The dots with error bars represent 10 equally spaced bins of averaged data, which are purely a visual aid to show the linear behavior.

4.6 Raman calibration

For rapid confirmation that such a high value of the channel sensitivity ratio coefficient C was feasible, we looked to the JET HRTS Raman scattering measurements during the same campaign. The measured data set is limited to just 4 useable plasma pulses, with the background calculated from separate vacuum shots. The measured Raman signal ratio is given by:

$$\frac{I_{R,\perp}}{I_{R,0}} = C\frac{N_{R,\perp}}{N_{R,0}} \quad (46)$$

$$C = \frac{I_{R,\perp}}{I_{R,0}} \cdot \frac{N_{R,0}}{N_{R,\perp}} \quad (47)$$

Here $I_{R,\perp}/I_{R,0}$ is the measured Raman ratio of the polarimetric and control channels, and $N_{R,\perp}/N_{R,0}$ is the ideal Raman ratio i.e. the ratio for equal sensitivity in both channels. The ideal ratio can be determined from the Muller matrix of rotational Raman scattering, calculated in [53] which gives:

$$\begin{aligned} M_{00} &= 13 + \cos^2\theta \\ M_{01} &= \sin^2\theta \\ M_{11} &= 1 + \cos^2\theta \end{aligned} \quad (48)$$

and following the same method as equation (45):

$$\frac{N_{R,\perp}}{N_{R,0}} = \frac{M_{00} - M_{11}}{2M_{00} + 2M_{01}} = \frac{3}{7} \quad (49)$$

Giving:

$$C = \frac{7}{3} \cdot \frac{I_{R,\perp}}{I_{R,0}} \quad (50)$$

We only have 4 useable Raman pulses to determine the sensitivity. The average measured values are $I_{R,\perp}/I_{R,0} = 2.88$ with a standard deviation of ± 0.78, giving $C_{Raman} = 6.72 \pm$

1.82. Despite the larger error, this value is consistent with the value determined by our measured polarimetric signal. Figure 33 shows an example of the Raman signal in the polarimetric and control channels. If the channel sensitivities were equal, according to equation (50) we should see the control signal peak more than twice as high as the polarimetric signal, whereas here instead it is about three times smaller. This confirms that there is a severe reduction in the sensitivity of the control channel.

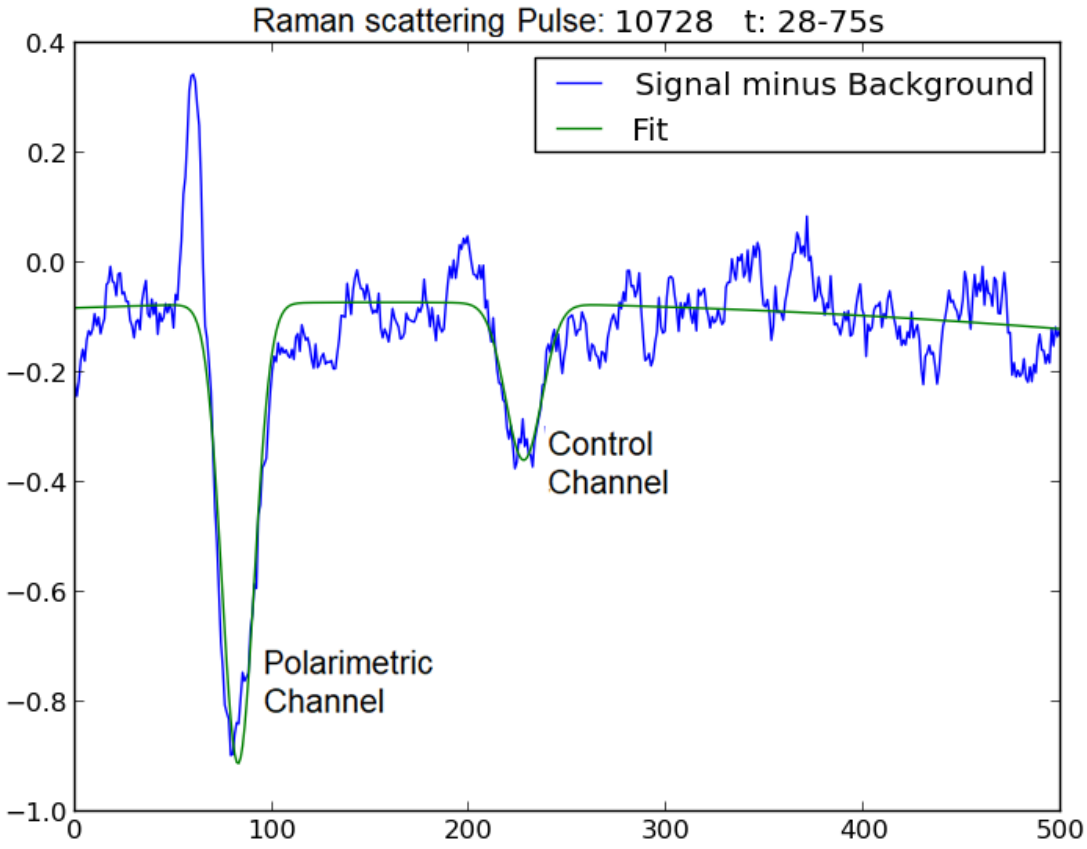

Figure 33. Example of a Raman scattering pulse, with laser segments averaged over the pulse duration to reduce noise.

4.7 Post-experiment spectral calibration

Post-campaign, to confirm the idea that the control channel fibres were misaligned, we attached a light source to the spectrometer side of the collection fibres to show the full alignment of the Torus Hall optics. Figure 34 shows images of the collection optics on top the JET machine (UMVP), these are the first main collection mirrors just above the collection window and lens. We can clearly see misalignment of the control channel fibres 127 and 128, compared to the well-aligned polarimetric channel fibre 124 (channel 125 was also well-aligned).

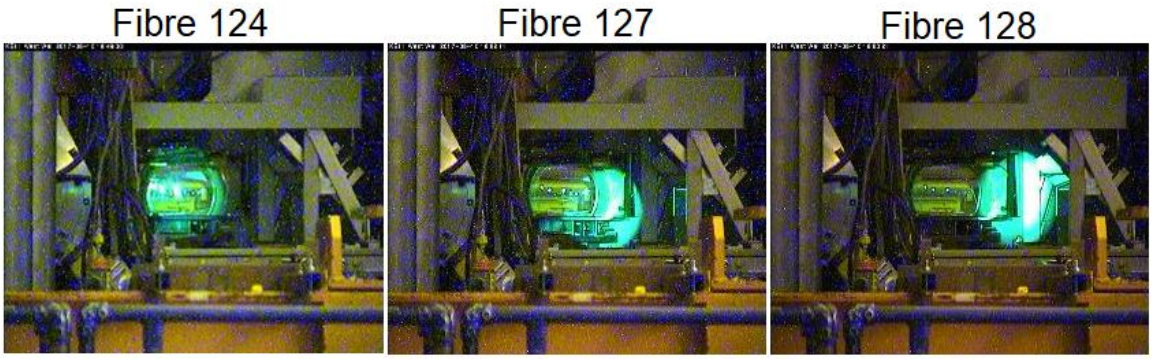

Figure 34. The misalignment of the control channel fibres 127 and 128, compared to the well-aligned polarimetric channel fibre 124.

Leaving the alignments untouched, a careful calibration of the fibre collection efficiency was been performed at the end of the experimental campaign. A full emission calibration was done with an in-vessel light source – a large integrating sphere with 100W tungsten light bulb (Figure 35).

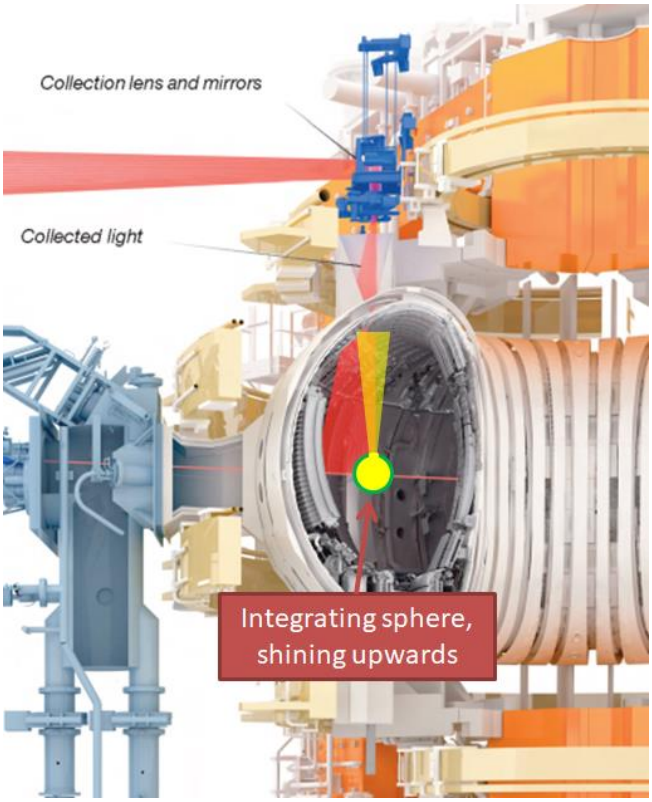

Figure 35. Depiction of post-experiment full emission calibration using a large integrating sphere tungsten light source.

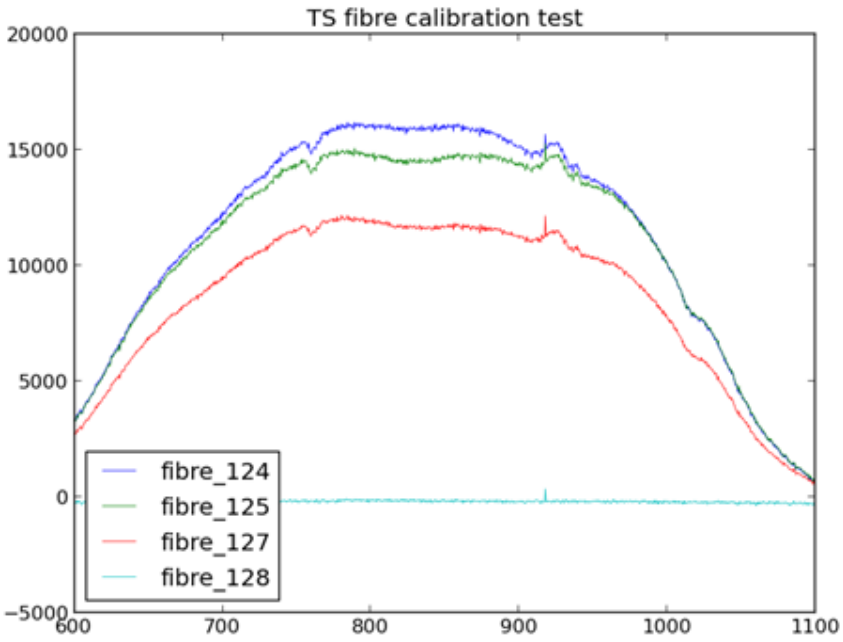

Figure 36. Fibre sensitivity recalibration measurements. The control pair were attenuated, particularity fibre 128.

Figure 36 shows the recalibrated spectral transmission of the polarimetric (124/125) and control (127/128) channels. We can see that fibre 128 is completely attenuated from the misalignment, while 127 is also affected. Performing an integration of these transmissions over the TS region (660-1050nm) gives the calibrated average sensitivity ratio as $C_{Cal} = 5.28 \pm 0.11$, which agrees with our original experimental measured $C_{Measured} = 5.45 \pm 0.77$.

Furthermore, the same ratio integrated over the Raman scattering range (1064±5nm) is $C_{Raman,Cal} = 5.82 \pm 0.12$. Taking this transmission factor into account with the measured C_{Raman} gives the relative measured $C_{Raman,Rel} = 6.09 \pm 1.65$ which, despite the large error is consistent with the measured $CM = 5.45 \pm 0.77$. These values are compared in table 3.

Method	*C value*	*Standard deviation*
$\boldsymbol{C_{Measured}}$	5.45	±0.77
$\boldsymbol{C_{Raman,Rel}}$	6.09	±1.65
$\boldsymbol{C_{Cal}}$	5.28	±0.11

Table 3. Sensitivity coefficient values from the experimental data ($C_{Measured}$), the value from the Raman calibration corrected with relative transmission factor ($C_{Raman,Rel}$), and the spectral calibration value (C_{Cal}).

A final test was performed to determine if the value of the system depolarization factor, $k = (8.61 \pm 2.37) \times 10^{-3}$, is reasonable. The main easily-measurable source of k is from the non-ideal behavior of the perpendicular polarizer, which allows a fraction of the main signal through, given by the value of its contrast ratio. The manufacturer's value of the contrast ratio was unavailable up to the laser wavelength of 1064nm, therefore a post-experiment calibration was also performed to determine the full spectral contrast ratio of the polarizer (Figure 37). Although the test performed is quite noisy, a contrast ratio of

~400 at 1064nm is a good approximation which accounts for about one third of the measured value of k. The remainder of the depolarization factor can be reasonably explained by the additional depolarization introduced by the other optical elements in the collection system (window, lens, mirrors).

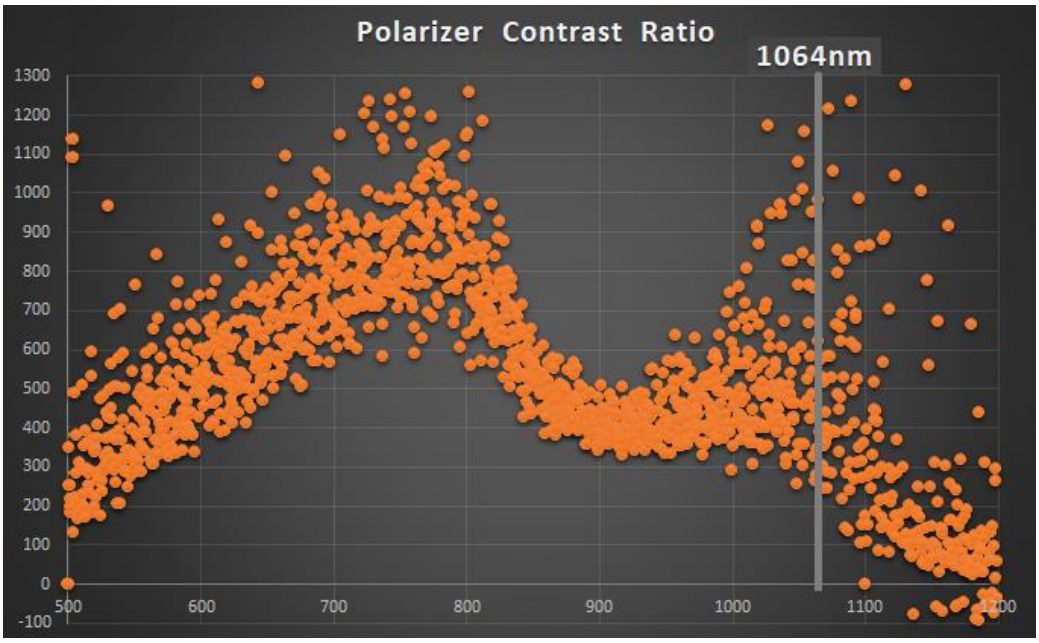

Figure 37. Spectral contrast ratio of the perpendicular polarizer installed in front of fibres 124 and 125.

4.8 Conclusions

During the second year of studies, we have successfully performed measurements of the depolarization of Thomson scattering radiation in the JET HRTS system. To our knowledge, this is the first time depolarized TS radiation has been measured in a magnetic fusion plasma, adhering to the established theory that the signal ratio has an approximately linear relationship with T_e.

The channel sensitivity ratio *C* and the depolarization factor *k* determined by the linear model fit of polarimetric data are consistent with the results of the Raman scattering and post-experiment calibrations, proving that the signal we have observed is actually the depolarization effect.

This technique is more suitable for high temperature plasmas, as the polarimetric signal and thus the accuracy increases with temperature. Despite this, our experiment showed that the polarimetric signal can also be detected for T_e < 10keV, by averaging over several laser pulses during a flat-top phase.

These results validate that polarimetric TS is a useful technique that can augment conventional TS or even be employed as an autonomous T_e measurement in high temperature plasmas such as those of ITER.

CHAPTER 5: DUAL LASER THOMSON SCATTERING IN LHD

This chapter describes the dual-laser Thomson scattering (TS) experiment undertaken in the Large Helical Device (LHD) stellarator in Toki, Japan during the third year of the doctoral studies; the results presented here are preliminary and collaboration with the Japanese team is ongoing.

The first ever testing of the dual-laser TS technique has been described in chapter 3. The major limitation of this first experiment was the closeness of the two laser wavelengths used, the selection of which was restricted by the relatively low plasma temperatures of RFX-mod. Here we describe the second experimental testing of the dual-laser technique, performed on LHD, a much larger device with temperatures high enough to use two lasers with well separated wavelengths. The personal work undertaken for this dual-laser experiment included onsite management of the data acquisition and initial data analysis. Although initially I was to perform an observatory role, the experimental lead physicist, E. Yatsuka, was unavailable to remain onsite after machine problems caused delays, and so this primary duty was afforded to me.

5.1 Dual-laser Thomson scattering

A severe limitation of the dual-laser experiment performed in RFX-mod [34] was the similarity of the available laser systems. As described previously, the dual-laser technique relies on having a measureable difference between the two overlapping scattered spectra. The Nd:YAG main laser (1064nm) and Nd:YLF calibration laser (1053nm) were often too spectrally close to have a measurable difference above the level of noise. Note that in RFX-mod there was also the availability of a ruby laser (λ = 694.3nm) and a second harmonic Nd:YAG laser (λ = 532nm) to use as a calibration laser, but the typical operational temperature of the device (< 1keV) was not hot enough to make these spectra overlap, which is required for comparison within the technique. The plasma temperatures in the larger LHD device can range from 5keV up to 20keV [54],

which means that we will have sufficient spectral overlap to use the onsite Nd:YAG (λ = 1064nm) as primary laser and an available ruby (λ = 694.3nm) as calibration laser. The motivation for the experiment is to test the dual-laser technique on a large device, with the improvement of using a more optimized laser selection.

5.2 Experimental set up

In contrast to the RFX-mod 90° scattering, the LHD Thomson scattering system (Figure 38) has a typical the scattering angle of 167° [54]. For this dual-laser experiment a 2J, 0.25Hz ruby laser (694.3nm) was installed to be used as the calibration laser, while the main laser was a 2J, 30Hz Nd:YAG (1064nm), which is also the primary laser used simultaneously for the conventional TS measurements in LHD. Both lasers were initially injected with a time delay of approximately 1ms, however this was reduced to ~500μs for the majority of the shots performed. As mentioned in chapter 3, in the RFX-mod experiment we allowed a maximum delay of 20μs for considering a laser pulse pair suitable for the dual-laser analysis. Such a small delay was not possible in LHD due to the limitations of the data acquisition system, however 500μs is still a reasonable delay value to consider T_e and n_e constant, given the MHD timescales in the more stable LHD plasmas [55].

The spectral channels of the standard LHD TS polychromators are not suitable for use with a ruby laser. For the purposes of this experiment, the spectral filters of single polychromator were modified to accommodate the ruby laser, with a single spatial channel (R = 3.583m) used for dual-laser calibration. A gold mirror is used as the collection mirror in the LHD TS system [56]. Figure 38 shows the product of gold reflectivity and transmission of each spectral channel in the polychromator, selected to reject ruby stray light. One difficulty was with spectral channel 3 (in blue), which can be seen from the figure to have a small transmission tail near the Nd:YAG laser line, and so receives a lot of stray light when the YAG fires. This channel was removed from the analysis when resolving the YAG spectrum, but was still fine to use when resolving the ruby spectrum.

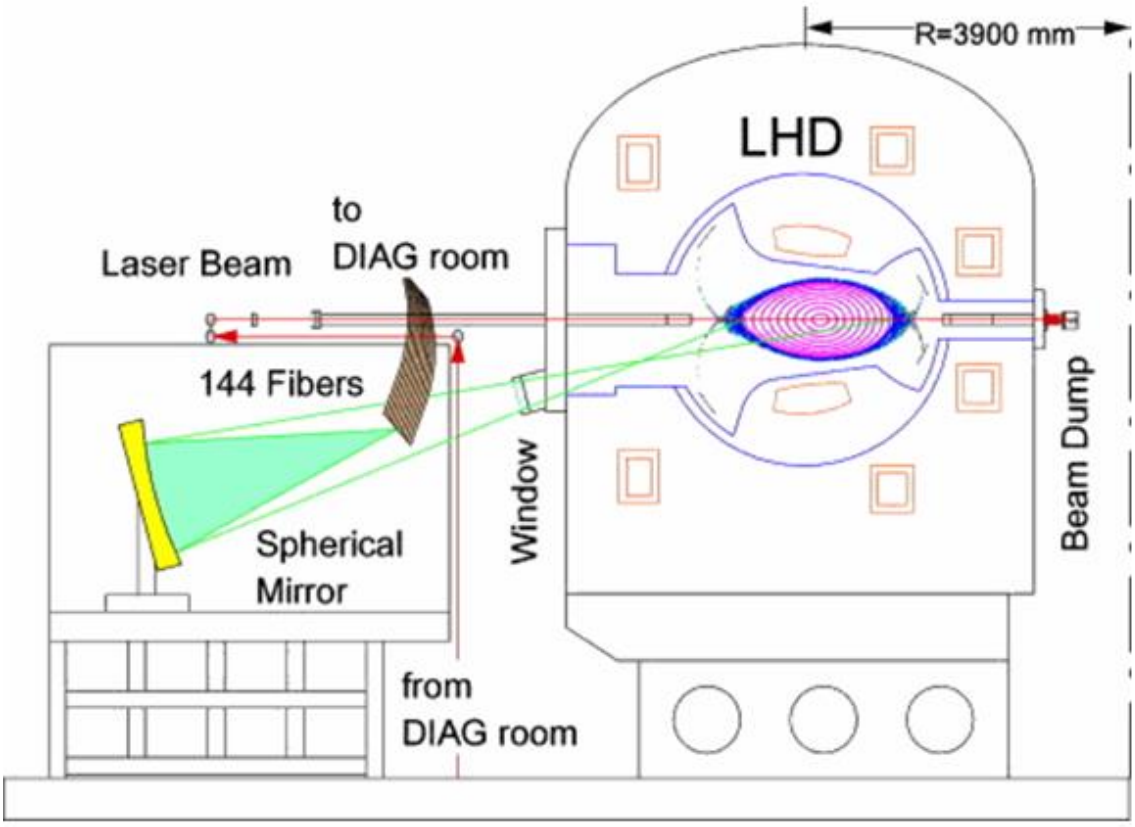

Figure 38. Schematic of the LHD Thomson scattering system **[57]**

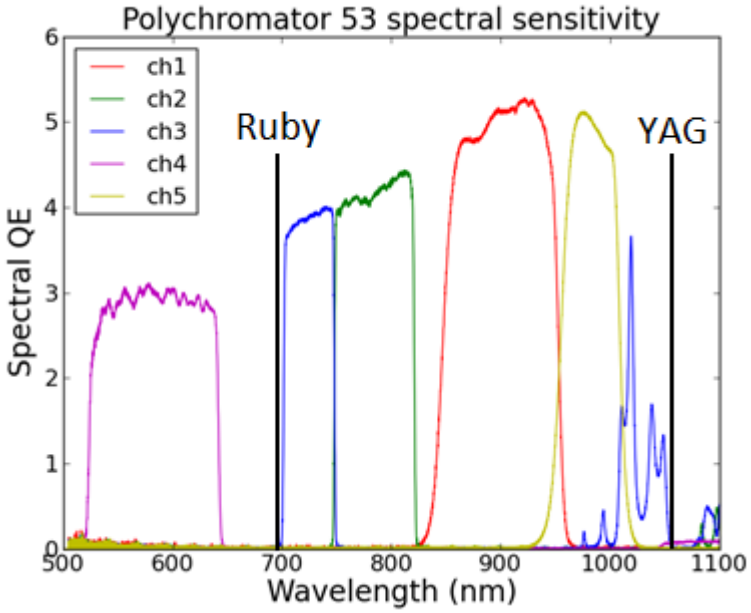

Figure 39. Transmission function of dual-laser calibration spectrometer, showing ruby and Nd:YAG laser lines.

The initial data acquisition was performed using two 4-channel oscilloscopes, the first receiving the signal from spectral channels 1-4 and the second for the channel 5 signal. This was cumbersome however, with the data needing to be manually saved and the spectrometers rearmed after every dual-laser shot. After the initial day of the experiment, a new data acquisition system was installed which allowed for continuous automatic measurement and data storage of all 5 channels. Figure 40 shows a dual-laser shot taken on the first oscilloscope and on the new device. Although the quality of the signal is much the same, the new device allowed for much more consistent acquisition.

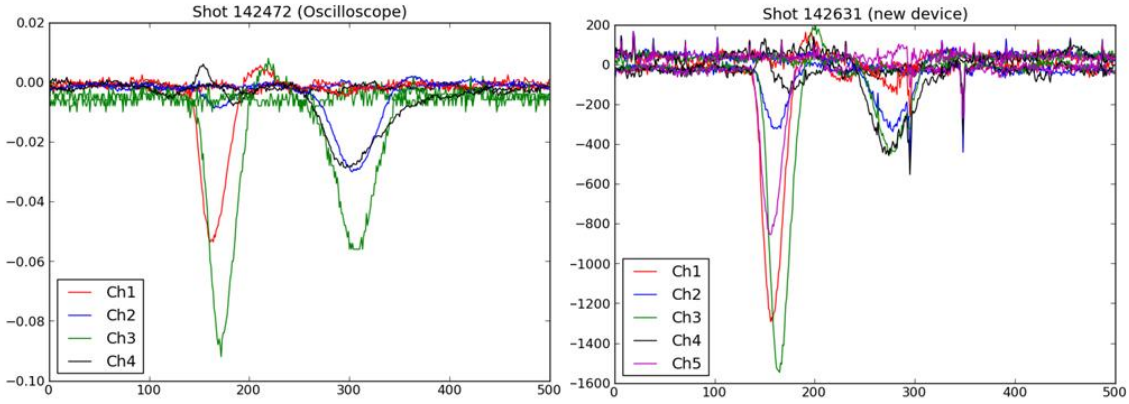

Figure 40. Dual-laser signals for the 4-channel oscilloscope (left) and new device (right). In both cases the Nd:YAG fired first with its signal on the left, and the ruby laser fired later with the peaks on the right.

5.3 Data analysis and preliminary results

Presented in this section is the full process of preliminary analysis of dual-laser (ruby and Nd:YAG) Thomson scattering for just one shot, LHD shot 142582 (Figure 41). Our analysis follows the method described in chapter 3 and in [34] and [47]. First, two separate fits of YAG and ruby signals are implemented using the conventional nonlinear TS two-parameter χ^2 minimization. These fits give two values of T_e and n_e (the latter in arbitrary units). Then a dual fit of the two sets of signals together is implemented by a 7-parameter (T_e , γ, and $A_C C_i$, $i = 1, \ldots 5$) non-linear minimization described by equations (28-30). Here, γ is the ratio of the total number of photons in the two spectra collected from the scattering volume, the $A_C C_i$ are 5 calibration factors of the relative spectral channel sensitivity. The original 7-parameter fit is solved for the $A_C C_i$ so that it reduces

to a 2-parameter nonlinear fit in γ and T_e, which is then solved by a 2D search. Initial guesses are the average T_e and γ from previous individual fits, provided they converged. The occurrence of a true minimum of the χ^2 for the dual fit is checked plotting the projections of the χ^2 surface around the minimum along the γ and T_e directions. This dual fit gives a unique value of T_e (Te_dual), of γ and 5 values of the calibration constants $A_C C_i$. From these data, five corrective factors CF_i are calculated to be applied to the original calibration factors C_i (see chapter 3). The steps of this procedure are as follows.

1) We have first processed the channel transmission functions (Figure 39). For simplicity we assumed that the transmission functions we obtained by the LHD TS team were corrected for the emission spectrum of the light source, so that they reflect exactly the relative sensitivity of the 5 spectral channels. If this is not the case the analysis should be repeated using the corrected functions. Recall also that channel 3 has been omitted from the YAG spectra reconstruction due to stray light.

2) From the recorded waveforms of shot 142582 we have applied a Gaussian fit to each peak to extract the signal values from the noise, and calculated the following set of signals in table 4.

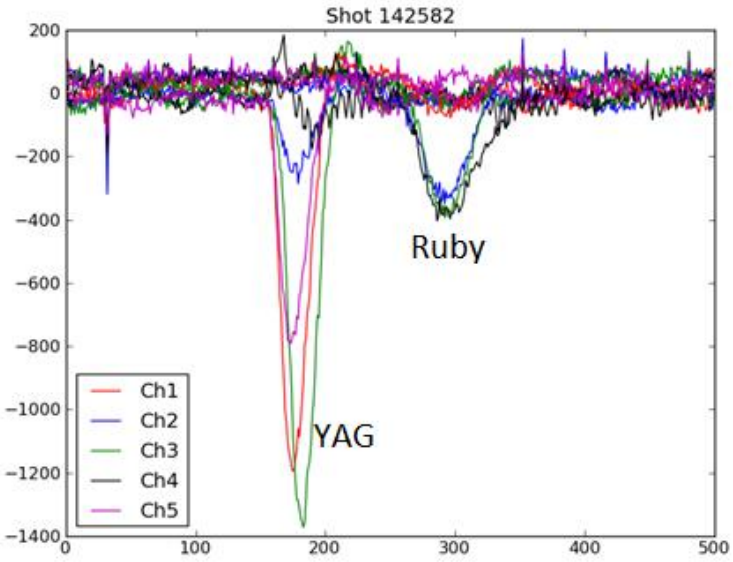

Figure 41. The 5-channel dual-laser spectra, with signals from the YAG laser on the left and the ruby laser on the right.

Channel	Ruby		YAG	
	Signal	Std. dev.	Signal	Std. dev.
1	5630.6	2848.0	28764.2	1222.9
2	20244.9	3918.1	5761.9	951.1
3	18656.3	2496.1	-	-
4	26483.0	4113.2	1864.6	1136.1
5	1005.1	913.0	18281.1	1065.9

Table 4. Calculated signal and standard deviations from Gaussian fits of the 5 channel waveforms (in arbitrary units).

3) These have been fitted separately using the Naito formulae described in section 2.2.4, assuming a scattering angle θ = 167˚. Figure 42 shows the results of the two fits. Here the x-axis is the normalized wavelength shift $x = (\lambda - \lambda_0)/\lambda_0$. The two fits give two different T_e values, as expected. The two spectra and the two signal sets are then plotted together as a function of the wavelength (Figure 43).

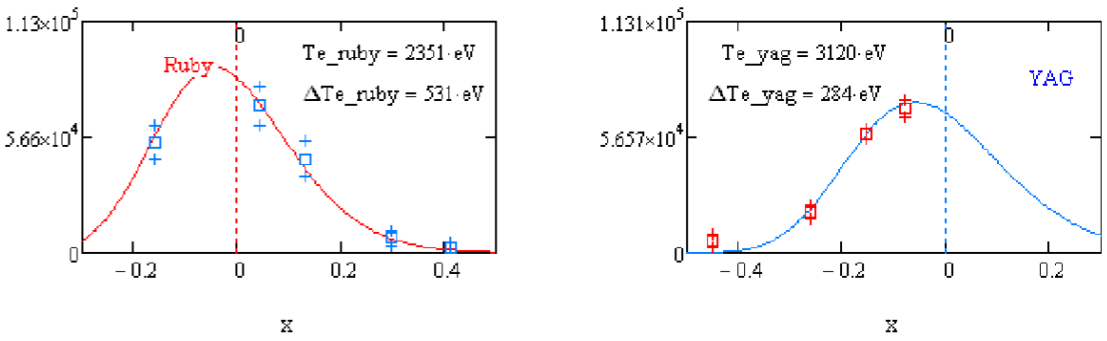

Figure 42. Individual fits of the two reconstructed laser spectra.

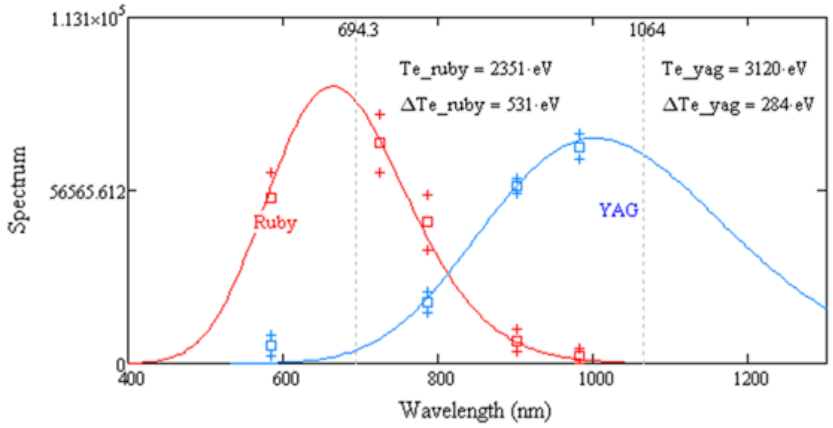

Figure 43. Ruby and YAG laser spectra as a function of wavelength.

4) We then implement the dual fit. Figure 44 shows the 2D surface and associated contour map of the dual χ^2 that includes both ruby and YAG signals. The variables of this fit are T_e and γ (the ratio between the areas of the individual spectra). The contour map shows clearly that there is a single minimum. This gives the final values of T_e (Te_dual) and γ. Subsequently the 5 values of the $A_C C_i$, corresponding to this minimum are calculated. Figure 45 plots the dual spectrum compared with the ruby and YAG data and with the two previously fitted spectra.

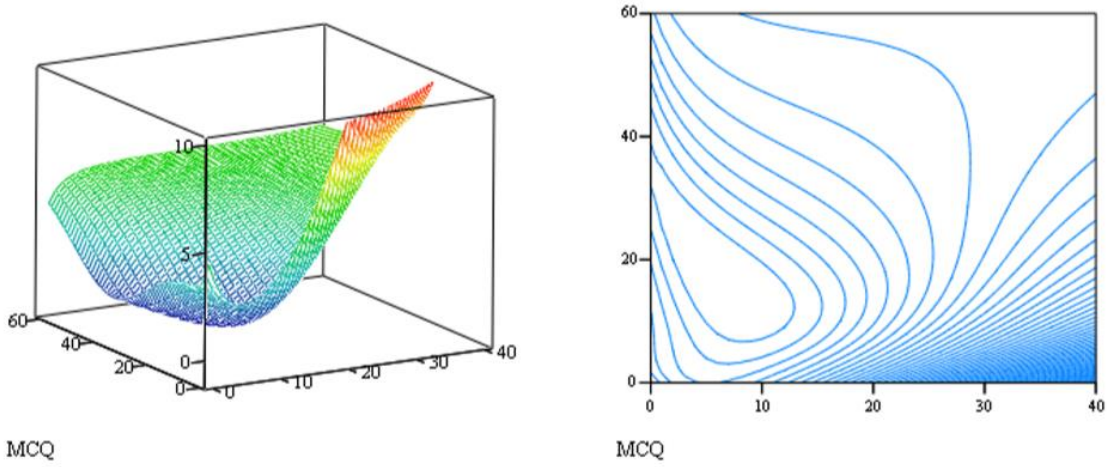

Figure 44. 2D surface and associated contour map of the dual fit χ^2 minimization that includes both laser signals.

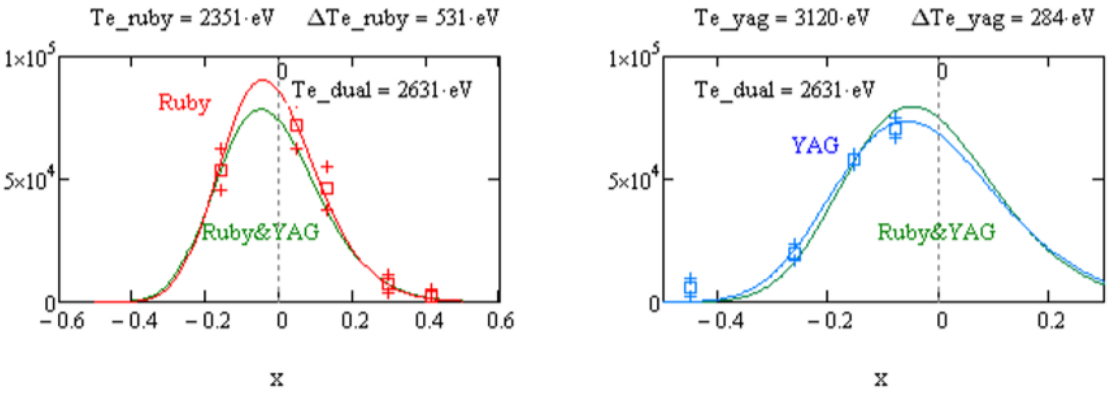

Figure 45. Comparison of the dual-laser fit with the previous individual fits of both laser spectra.

5) From the results of the dual fit we find the correction factors CF_i of the relative calibration constants; we apply them to the ruby and YAG signals and plot them together with the dual fit spectrum in Figure 46. The corrected data points fall very close to the spectrum indicating that the procedure is correct.

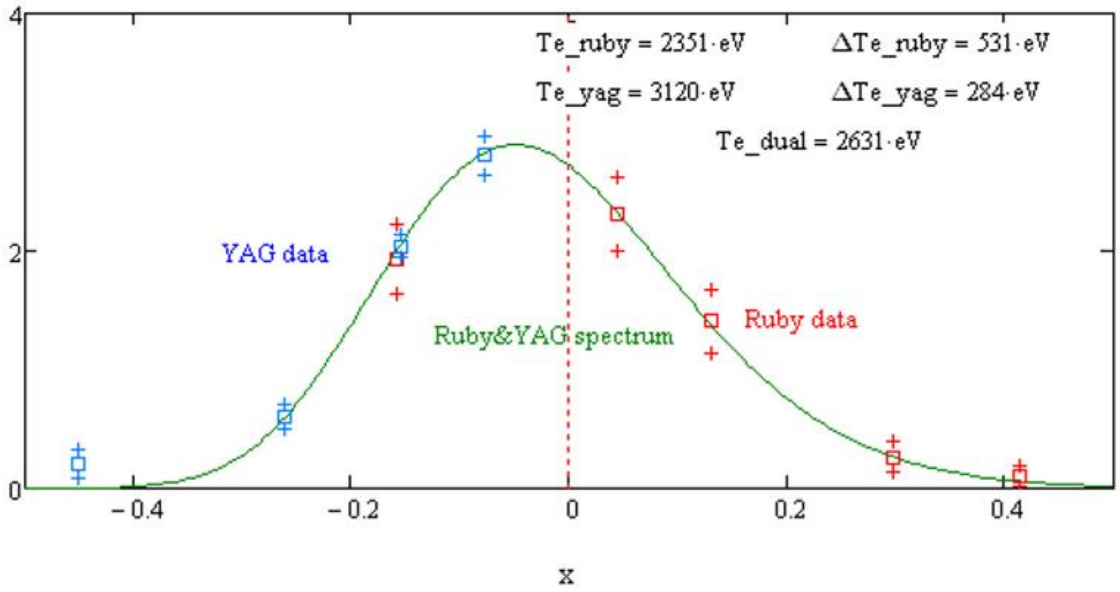

Figure 46. The dual-fit spectrum with correction factors $\boldsymbol{CF_i}$ applied to both laser signal data.

As a final part of the preliminary analysis, we have performed the above procedure on the majority of the obtained data. The data set was limited to data measured with the new acquisition system, with the same laser delay of ~500ms, and finally data where both individual fits converged. These criteria reduce our useable data set to ~90 laser pulses with which we can perform a statistical analysis. Figure 47 shows the correction factors for the Nd:YAG primary laser across spectral channels 1, 2, 4 and 5 of the spectrometer. Table 2 shows the averaged values and standard deviations of these correction factors for the, calculated individually for each pulse as in chapter 3, $CF_i = A_M C_i SM(T_e^{dual})/ A_M^p C_i^p SM(T_e^{yag})$.The correction factors of each spectral channel are all close to 1, which implies the original calibration coefficients C_i^p are still acceptable. Channel 4 shows large error which is expected as it is the channel furthest from the YAG laser line and rarely receives YAG scattering signal above noise level. Channel 2 is the next furthest from the YAG line and so has reduced signal-to-noise and more error that channels 1 and 5. We

highlight again that this is a preliminary analysis and some assumptions may need to be modified and recalculations made, though the process will remain the same.

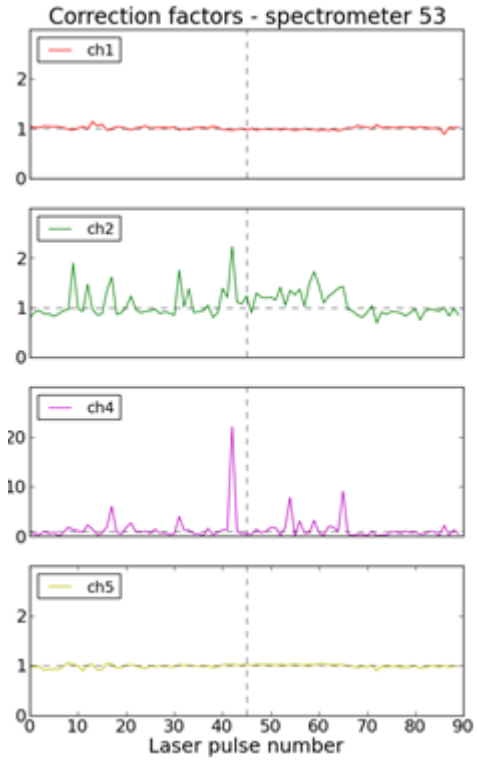

Figure 47. The correction factors $\boldsymbol{CF_i}$ for the main laser in the spectrometer across the four useable spectral channels.

Channel	*Correction factor*	*Standard deviation*
1	1.008	0.033
2	1.067	0.270
4	1.387	2.607
5	0.989	0.032

Table 5. Average values with standard deviations of the correction factors CF_i for the relative calibration coefficients C_i^p of the main YAG laser across the four useable spectral channels.

5.4 Conclusions

During the third year of studies, we have carried out the testing of the dual-laser self-calibrating TS technique in the LHD stellarator in Japan. This experiment is the second testing of the technique. It builds on the first experimental test, performed in RFX-mod and described in chapter 3. This larger device with higher temperatures allowed for a much more favourable selection of main and calibration lasers, which was the major limitation of the first test. Preliminary analysis suggests that the ruby/YAG dual-laser fit has a much higher χ^2 convergence success rate with better signal-to-noise than the YLF/YAG pairing in RFX-mod.

This preliminary analysis, carried out with the methodology of the first test, builds on the previous RFX-mod experiment and suggests that reliable measurements of the calibration coefficients can be obtained with a statistical analysis of a reasonable number of laser shots with a good signal-to-noise ratio. Some assumptions made may have to be modified; further analysis and collaboration with the LHD team is ongoing.

SUMMARY AND PROSPECTS

Two previously untested advanced Thomson scattering techniques have been experimentally demonstrated, on three separate fusion devices. This thesis has described the methodology and results of all three experiments, as well as presenting the necessary Thomson scattering theoretical background.

The first known recorded testing of the self-calibrating dual-laser technique was performed in RFX-mod, Padova. My personal contribution to this experiment included the design, installation and testing of the beam combiner optical system, the data analysis, and the publication of the results as first author [34]. Despite the limitations of the setup, particularly regarding device temperature and laser selection, reliable measurements of the calibration coefficients can be obtained with a statistical analysis of a reasonable number of laser shots with a good signal-to-noise ratio.

The second recorded testing of this technique was performed in LHD, Toki, Japan. This hotter device enabled a much more favourable selection of lasers, producing a data set with a much improved signal-to-noise ratio. My personal contribution to this experiment was onsite data collection and experiment management, and data analysis. Although the analysis and collaboration is ongoing, preliminary results further demonstrate the feasibility of this technique. This self-calibrating technique is unobtrusive and removes the requirement for traditional recalibration of the optics, which is invasive and a real challenge in larger devices such as ITER where remote handling and regular recalibration may be required.

The first known experiment to measure the depolarization of Thomson scattering radiation was performed in JET, Oxford. This depolarization effect is the basis of the polarimetric Thomson scattering technique. My personal contribution to this experiment included the modification and installation of a Thomson scattering spectrometer, onsite data acquisition, data analysis, and expected publication of results as co-author [48]. We have proven the depolarization signal is present, consistent with the theory, and furthermore measureable at temperatures below 10keV with appropriate use of signal averaging. We have demonstrated the feasibility of the technique, which could provide an

additional independent electron temperature and density measurement competitive in accuracy with conventional Thomson scattering in high temperature plasmas.

These results are significant, as both of these techniques are of high value and interest for the next generation of fusion devices, and are being considered in the design of the ITER Thomson scattering systems. The dual-laser calibration technique has been suggest in ITER via the integration of a secondary laser at λ = 1340nm (primary laser λ = 1064nm) [58]. This secondary laser is already being considered to aid with maintaining the system accuracy in high T_e, low n_e conditions, and so to configure this laser to also perform the self-calibration measurements could be of great usefulness with minimal investment.

The polarimetric Thomson scattering technique has been proposed for ITER by way of a "hybrid Thomson scattering" scheme, wherein the conventional and polarimetric TS measurements are integrated into the same system [59]. The conventional TS polychromator would receive the polarized major component of the scattered light and perform the conventional spectral channel analysis. At the same time a polarizing beam splitter situated before the polychromator would separate the depolarized component for polarimetric TS analysis, which would feed into an extra channel of the same polychromator (figure 48). This would be an elegant solution and could provide a much desired increase in accuracy at high temperatures for relatively small investment.

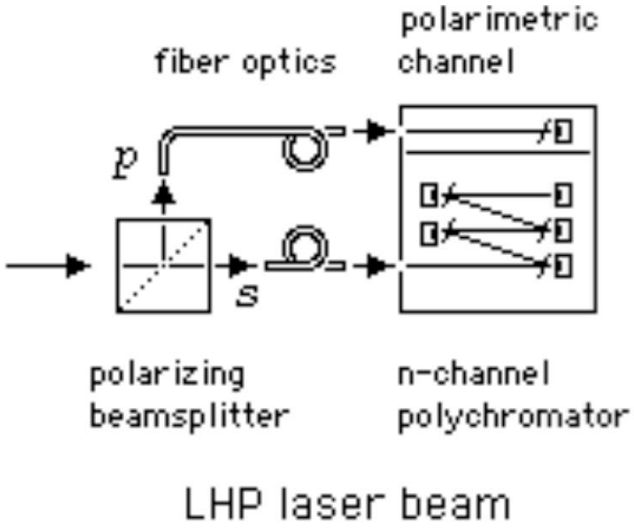

Figure 48. Proposed ITER hybrid Thomson scattering system for linearly polarized (LHP) laser input, integrating a polarimetric channel into the conventional TS system by separating the polarized and unpolarized components of the scattering signal [59].

REFERENCES

[1] **BP** Statistical Review of World Energy. 2017.

[2] **Boden T A, Marland G, Andres R J.** *Global, Regional, and National Fossil-Fuel CO2 Emissions.* U.S. Department of Energy, 2017.

[3] **UNFCC**. *The Paris Agreement*. United Nations Framework Convention on Climate Change, 2015.

[4] **Bethe H A, Critchfield C L.** 1938, Physical Review, Vol. 54, pp. 248-54.

[5] **Rhodes R.** *Dark Sun: the making of the hydrogen bomb*. 1995.

[6] **efda.org**. Figure 1 (left). [Online] 2011. http://www.efda.org/2011/09/tokamak-principle-2/.

[7] **pppl.gov**. Figure 1 (right). [Online] 2005. http://en.wikipedia.org/wiki/File:Tokamak_fields_lg.png.

[8] **Hawryluk R J, et al**. s.l. : Nucl. Fusion, 2009, Vol. 49. 065012.

[9] **Dept. Energy & Climate Change**. *Digest of United Kingdom Energy Statistics 2011*. 2011.

[10] **Boozer A H.** Rev. Mod. Phys., 2004, Vol. 76. 1071.

[11] **mpg.de.** Figure 2 (left). [Online] 2008. http://einstein-virtuell.mpiwg-berlin.mpg.de/VEA/SC563727255_MOD1878792365_SEQ1100154683_SL1183723362_en.html.

[12] **cea.fr**. Figure 2 (right). [Online] http://www-fusion-magnetique.cea.fr/gb/fusion/principes/principes02.htm.

[13] **iter.org**. [Online] 2011. https://www.iter.org/.

[14] **kit.edu**. Figure 3 (left). [Online] 2010. http://www.ihm.kit.edu/97.php.

[15] **nupex.eu**. Figure 3 (right). [Online] 2017. http://nupex.eu/index.php?g=textcontent/nuclearenergy/nuclearfusion&lang=en.

[16] **McCraken G, Stott P.** *Fusion: The Energy of the Universe*. 2013.

[17] **Hutchinson I H**. *Principles of plasma diagnostics second edition*. Cambridge, 2002.

[18] **Prunty S L**. Figure 7. *A primer on the theory of Thomson scattering for high-temperature fusion plasmas.* Phys. Scr., 2014, Vol. 89. 128001.

[19] **euro-fusion.org**. Figure 8. [Online] 2011. https://www.euro-fusion.org/wpcms/wp-content/uploads/2011/07/spectra-m.png.

[20] **Eubank A, Sindoni E**. *Course on Plasma Diagnostics and Data Acquisition Systems*. C.N.R - Euratom - Editrice Compositori Bologna, 1975.

[21] **Stejner M, et al**. *Plasma rotation and ion temperature measurements by collective Thomson scattering at ASDEX Upgrade*. Plasma Phys. Control. Fusion, Vol. 57. 062001.

[22] **Theimer O, Hicks W**. *Depolarization of light scattered by a relativistic plasma*. Phys. Fluids, 1968, Vol. 11. 1045.

[23] **Orsitto F, Tartoni N**. *Proposal for a new electron temperature diagnostic for fusion reactors.* Rev. Sci. Instrum., 1999, Vol. 70. 798.

[24] **Zhuravlev V A, Petrov G D**. Soviet J. of Plasma Phys., 1979, Vol. 5. 3.

[25] **Selden A C**. Simple analytical form of the relativistic Thomson scattering spectrum. Physical Letters, 1980, Vol. 79A. 5,6.

[26] **Matoba T, Itagaki T, Yamauchi T, Funahashi A.** Japan. J. Appl. Phys., 1979, Vol. 18. 1127.

[27] **Naito O, Yoshida H, Matoba T**. *Analytical formula for fully relativistic Thomson scattering spectra.* Phys. Fluids B, 1993, Vol. 5. 4256–8.

[28] **Giudicotti L, Pasqualotto R**. *Dual-laser calibration of Thomson scattering systems in ITER and RFX-mod.* Nucl. Fusion, 2014, Vol. 54. 043005.

[29] **Smith O R P, Gowers C, Nielsen P, Salzmann H.** *A self-calibration technique for a Thomson scattering system.* Rev. Sci. Instrum., 1997, Vol. 68. 725–7.

[30] **Tojo H, Hatae T, Itami K**. *An in-situ relative calibration method for Thomson scattering diagnostics using a double-pass scattering system*. Plasma Fusion Res., 2011, Vol. 6. 1302018.

[31] **Tojo H, Ejiri A, Hiratsuka J, Yamaguchi T, Takase Y, Itami K, Hatae T**. *First measurement of electron temperature from signal ratios in a double-pass Thomson scattering system*. Rev. Sci. Instrum., 2012, Vol. 83. 023507.

[32] **Tojo H, Hatae T, Itami H**. *Principle of an in-situ relative calibration method using a double pass beam for Thomson scattering diagnostics*. J. Instrum., 2012, Vol. 7. C05004.

[33] **Tojo H, Yamada I, Yasuhara R, Ejiri A, Hiratsuka J, Togashi H, Yatsuka E, Hatae T, Funaba H, Hayashi H, Takase Y, Itami K**. *Validations of calibration-free measurements of electron temperature using double-pass Thomson scattering diagnostics from theoretical and experimental aspects*. Rev. Sci. Instrum., 2016, Vol. 87. 093502.

[34] **McCormack O, Giudicotti L, Fassina A, Pasqualotto R**. *Dual-laser, self-calibrating Thomson scattering measurements in RFX-mod*. Plasma Phys. Control. Fusion, 2017, Vol. 59. 055021.

[35] **Giudicotti L, Bassan B, Orsitto F P, Pasqualotto R, Kempenaars M, Flanagan J**. *Conceptual design of a polarimetric Thomson scattering diagnostic in ITER*. Journal of Instrumentation, 2016, Vol. 11.

[36] **Beausang K.** *The consistency of electron temperature measurements by Thomson scattering at the JET tokamak*. Cork, Ireland : Ph.D. thesis University College Cork, 2011.

[37] **Giudicotti L**. *Polarimetric Thomson scattering for high Te fusion plasmas*. Prague, CZ : Laser Aided Plasma Diagnostics 18, 2017.

[38] **Collett E**. *Polarized Light. Fundamentals and Applications*. Marcel Dekker, 1993.

[39] **Segre S E, Zanza V**. *Polarization of radiation in incoherent Thomson scattering by high temperature plasma.* Phys. Plasmas, 2000. Vol. 7. 2677.

[40] **Parke E, Mirnov V V, Den Hartog D J.** *A polarization-based Thomson scattering technique for burning plasmas.* 2014 JINST 9 C02030.

[41] **Kurskiev G S, Sdvizhenskii P A, Bassan M, Andrew P, Bazhenov A N, Bukreev I M, Chernakov P V, Kochergin MM, Kukushkin A B, Kukushkin A S, Mukhin E E, Razdobarin A G, Samsonov D S, Semenov V V, Tolstyakov S Yu, Kajita S, Masyukevich S V**. *A study of core Thomson scattering measurements in ITER using a multi-laser approach*. Nucl. Fusion, 2015, Vol. 55. 053024.

[42] **Hare D**. *Investigation of validity of dual laser self-calibration of Thomson scattering on ITER UKAEA.* Culham Report 28 June 2005, 2005.

[43] **Pasqualotto R, Giudicotti L, Alfier A, Walsh M J**. *Calibration methods for ITER core LIDAR*. J. Phys.: Conf. Ser., 2010, Vol. 227. 012044.

[44] **Yatsuka E, Hatae T, Kusama Y**. *A self-calibration method for edge Thomson scattering Diagnostics in ITER*. J. Plasma Fusion Res. Ser., 2010, Vol. 9. 12–17.

[45] **Alfier A, Pasqualotto R**. New Thomson scattering diagnostic on RFX-mod. Rev. Sci. Instrum., 2007, Vol. 78. 013505.

[46] **Franz P, Gobbin M, Marrelli L, Ruzzon A, Bonomo F, Fassina A, Martines E, Spizzo G.** *Experimental investigation of electron temperature dynamics of helical states in the RFX-Mod reversed field pinch*. Nucl. Fusion, 2013, Vol. 53. 053011.

[47] **Giudicotti L, Pasqualotto R, Fassina A**. *Dual-angle, self-calibrating Thomson scattering measurements in RFX-mod*. Rev. Sci. Instrum., 2014, Vol. 54. 043005.

[48] **Giudicotti L, Kempenaars M, McCormack O, Flanagan J, Pasqualotto R, JET contributors**. *First observation of the depolarization of incoherent Thomson scattering radiation from a fusion plasma*. (Submitted for publishing), 2017.

[49] **Mirnov V V, Den Hartog D J, Parke E**. *Exact relativistic expressions for polarization of incoherent Thomson scattering*. Phys. Plasmas, 2016, Vol. 23. 052108.

[50] **Mirnov V V, Den Hartog D J**. *Polarization of incoherent Thomson scattering for electron temperature measurement*. Plasma Phys. Control. Fusion, 2017, Vol. 59. 063001.

[51] **Bassan M, Andrew P, Kurskiev G, Mukhin E, Hatae T, Vayakis G, Yatsuka E, Walsh M.** *Thomson scattering diagnostic systems in ITER*. 2016 JINST 11 C01052.

[52] **Pasqualotto R et al**. *High resolution Thomson scattering for Joint European Torus (JET)*. Rev. Sci. Instrum., 2004, Vol. 75. 3891.

[53] **Giudicotti L, Pasqualotto R**. *Rotational Raman scattering as a source of polarized radiation for the calibration of polarization-based Thomson scattering*. Plasma Phys. Control. Fusion, 2015. Vol. 57. 035001.

[54] **Yamada I et al**. *Calibration of the LHD Thomson scattering system*. Rev. Sci. Instr., 2016, Vol. 87 (11). 11E531.

[55] **Ichiguchi K et al**. *Multi-scale MHD analysis of LHD plasma with background field changing*. Nucl. Fusion, 2015, Vol. 55. 043019.

[56] **Narihara K et al**. *Development of Thomson scattering diagnostics for the large helical device.* Fusion Engineering and Design, 1997, Vols. 34-35. 67-72.

[57] **Yamada I, Narihara K, Funaba H, Hayashi H, Kohmoto T, Takahashi H, Shimozuma T, Kubo S, Yoshimura Y, Igami H, Tamura N**. *Improvements of data quality of the LHD Thomson scattering diagnostics in high-temperature plasma experiments.* Rev. Sci. Instr., 2010, Vol. 81. 10D522.

[58] **ITER Internal Report**. *Calibrations for ITER Core Plasma TS.* 2017, ITER D Q5U6YP v2.1

[59] **L. Giudicotti.** *Polarimetric Thomson scattering for high Te fusion plasmas.* 2017 JINST 12 C11002.